Towards the next generation of 3D printing method for printing microfiltration membranes

Shang-Che Wu

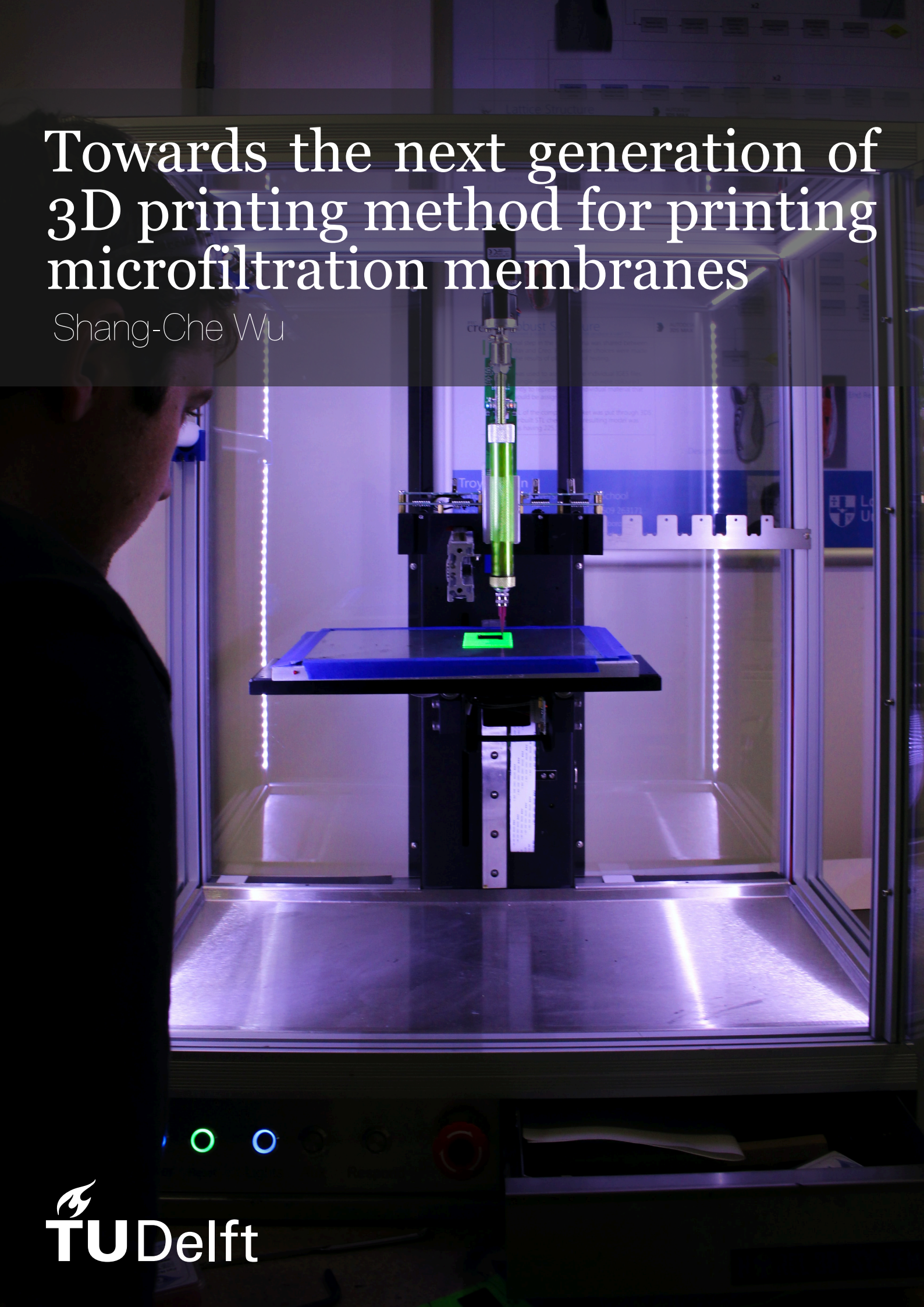

TU Delft

Towards the next generation of 3D printing method for printing microfiltration membranes

by

Shang-Che Wu

to obtain the degree of Master of Science in Mechanical Engineering
at the Delft University of Technology.

Student number:	5240352	
Thesis Committee:	Dr. H. Bazyar,	TU Delft, Supervisor
	Dr. A. Kostenko	Photosynthetic. B.V., Supervisor
	Dr. Ir. T. J. H. Vlugt,	TU Delft
	Dr. M. J. M. Mazandarani,	TU Delft
Additional supervisor:	Ir. W. A. van Vliet,	Photosynthetic B.V.

Cover: 3D printer photograph by Rob Wingate under Unsplash License
Style: TU Delft Report Style, with modifications by Daan Zwaneveld (modified)

TU Delft

Acknowledgements

"What does not kill you makes you stronger"
– Friedrich Nietzsche

This was a long journey, too many things went wrong, and too much stuff was puzzling to everyone. However, throughout this process, we learned bit by bit about what we don't know (in terms of science) and what can be improved on, I think in the end we achieved something that was still interesting, although not quite decisive, and the interesting part is all that matters.

First and foremost, I would like to thank my parents for their continuous and generous financial support, without their understanding and help, I would not be able to continue this project. I would also like to thank Heather for her emotional support, as she stands my complaints (almost) every day and continuously support me to push on with my project.

I would also like to thank my supervisors, Hanieh, Wesley, and Alex. Thank you Hanieh for the continuous positive attitude that you continue to instill in me, and for trusting that I can finish the project in an orderly manner. Without your help and suggestions in all directions, this project cannot and will not be finished. Thank you Wesley for the help in printing and the occasional crash courses in chemistry. I have to admit I do not understand everything, but your help on the printing side has been immense, and I will look back fondly to our chats here and there when we are both in the lab. Thank you Alex for patiently answering me when I keep bugging you about how the printer works, this definitely has given me some insight into how everything works and how things can be improved on. Additionally, I would like to thank the photosynthetic team, especially Mark, for their continuous technical and research support.

Additionally, I would like to thank Thejas and Georgia, for joining the discussions on permeability, these discussions gave me more understanding of how permeability is calculated and where further research is needed. I would also like to thank here Dagney for her help, not only in measuring the absorbance of HABI and CQ, but also her chats and comforting words during the first half of the project. I would like to thank Agnieszka for her help in AFM measurements, Waqas for his help in particle size distribution measurement, and DEMO TU Delft for helping me manufacture the filtration and permeability membrane cell.

Finally, I would like to thank all my friends, Rathish, Marlena, Louis... just to name a few, for supporting me throughout this journey. It has been a long time coming.

Shang-Che Wu
Delft, March 2023

Abstract

Current membrane fabrication processes are not sustainable as they are energy-intensive and require hazardous solvents. Additive manufacturing, due to its low waste production and the absence of harmful chemicals, can provide a more sustainable membrane manufacturing process. Up to this point, there was no way to 3D-print a membrane that meets the microfiltration pore sizes (1-10 μm) required in today's industry. In this work, we showcase for the first time that membrane with pore size < 10 μm can be 3D-printed via a dual wavelength 3D printer. Polyethylene Glycol Diacrylate (PEGDA) hydrophilic membranes with cylindrical pores were designed and printed.

A dual-wavelength micro-stereolithography 3D printer has been employed to print the membranes. Photopolymerizable resins containing PEGDA monomers, were polymerized into membranes via a mixed projection of UV and blue light, creating unpolymerized pores and polymerized matrix respectively.

Using a pixel size of 1.4 μm, we could produce hydrophilic membranes with cylindrical pores and a diameter < 10 μm. These membranes were compared with benchmarking commercial PTFE membranes (JCWP14225, Merck, Germany) with the same pore size range. The resulting membranes exhibited good oil-repellent properties, indicated by the higher oil contact angle values under water. The permeability and filtration results also provide valuable insights into the material used for membrane printing. All in all, a successful microfiltration membrane has been produced via a fast, user-friendly and sustainable method.

We have introduced the next-generation 3D printing method for printing microfiltration membranes with precise pore size, shape, configuration, and arrangement. With further improvements, this technology will provide a new era in membrane manufacturing.

List of Figures

List of Tables

Contents

1

Introduction

A membrane, as defined in *industrial separation processes* is ”A semipermeable phase, which restricts the motion of certain species in a different way[1],” or as German researcher Mathias Ulbricht puts it, membranes are ”interfaces between two adjacent phases acting as a selective layer, regulating the transport of substances between two compartments[2].” As defined, Membranes are used in industrial processes for separating two different kinds of phases. It has the advantage of, when compared to other chemical processes, not requiring any additives, while also having a low energy consumption, making membranes a perfect candidate for green and sustainable process engineering[3].

The same however, can not be said about membrane production, as it is an energy intensive, sometimes even hazardous process. The production process heavily relies on non-biodegradable or even hazardous solvents, they thus exacerbate the energy crisis and can cause harm to workers and the environment during production[4]. Hence, a new solution of producing membranes must be developed and utilized.

1.1. Introduction to Membranes

In general, membranes are classified by the separation process they are applied in and also the pore sizes of the membranes itself, which affects the size of the particles that can be separated. Membranes can be categorized, using this definition, into four different types of membranes[1]: *Microfiltration* (MF), *Ultrafiltration* (UF), *Nanofiltration* (NF) and *Reverse Osmosis* (RO); with microfiltration membranes having the largest pore sizes with a range of 0.1-10 μm. A figure explaining the difference visually is given as Figure 1.1.

Membrane technology has been applied to a lot of aspects of modern human life, from large desalination plants using reverse osmosis membranes, to food factories using membranes for wastewater treatment, to even drug delivery systems smaller than the size of a human body[5]. Figure 1.2 shows a typical water treatment unit, in which a microfiltration membrane unit has been incorporated[6]. The applications are plenty and new ways of using membranes are being researched and applied all the time.

Currently, common membranes are made of polymers, and to a lesser extent, ceramics[7]. Metallic[5] and zeolite[8] membranes also exist, however to limit the scope of the discussion they will

be excluded in the following sections. Common materials include polysulfone (PSU) and poly(vinylidene difluoride) (PVDF), with their industrial process procedure well optimized in an age where there was less concern for environmental issues[7].

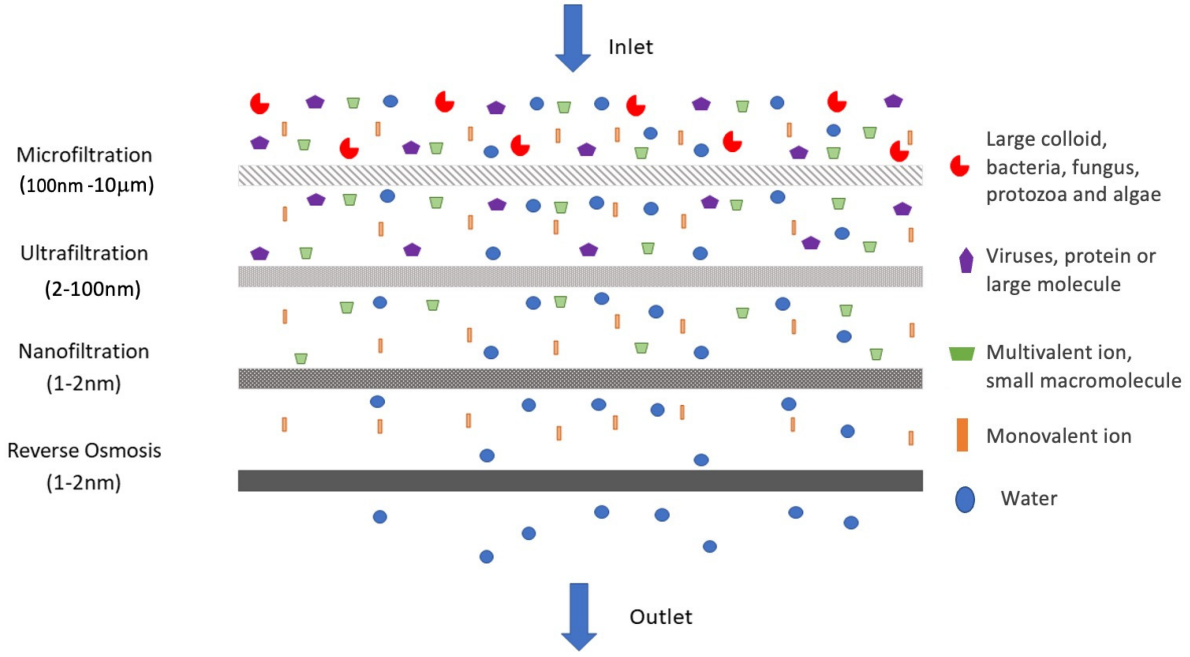

Figure 1.1: Membrane categories defined by their pore sizes and examples of biological particles that can be filtered[9]

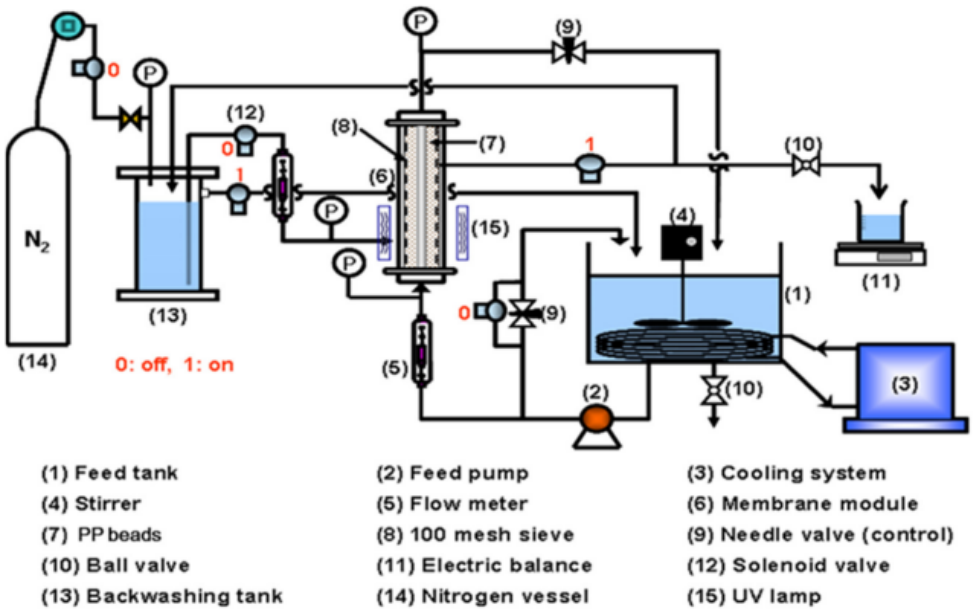

Figure 1.2: An example of a typical water treatment unit, the membrane shown here is an MF unit[6].

1.2. Conventional Membrane Production

We outline here some of the conventional methods of producing membranes.These common methods of membrane production include: phase inversion, track-etching, electrospinning and sintering[10,11].

1.2.1. Phase Inversion

The most commonly used phase inversion method, and also the most commercialized method of membrane production[11], is non-solvent induced phase separation (NIPS). In the NIPS method, a solution of polymer mixed with solvent is first made, this is normally refered to as the dope solution, or dope. Then using a knife or dye, the dope is spread into a thin film. The thin film is then immersed in a non-solvent bath, the organic solvent will exchange with the non-solvent and hence a membrane can be formed[12]. The process is shown in Figure 1.3a.

Another commonly used method for membrane is the thermal induced phase separation (TIPS). In this process, the polymer is mixed with the solvent, with the mixture being at a very high temperature. The dope is then cooled or quenched, inducing phase separation, which separates the solution into a polymer-rich and a polymer-lean phase, giving rise to the membrane walls and pores, respectively[13].The process is depectied in Figure 1.3b

These methods however, normally requires using toxic solvents, which would both present harm to humans and the environment. Another downside of phase inversion methods are that the morphology of the membrane cannot be directly controlled, and many experimental parameters, such as the temperature of the solvent/non-solvent or the viscosity of the fluids, will have a large effect on the final product[14].

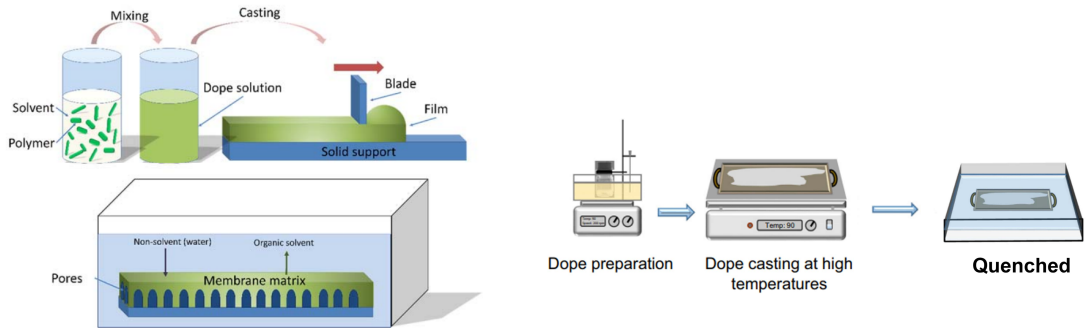

Figure 1.3: (a) The non-solvent phase separation (NIPS) process[12] (b) A typical thermal induced phase separation (TIPS) process[15]

1.2.2. Track Etching

The track etching method relies on ion irradiation, in which an or multiple ion dose(s) are injected into a polymer solid, leaving behind an ion track[16]. The ion damaged polymer is then put into an etchant bath, in which the etchant will create pores through the polymer parts that were damaged by the ions (ion tracks)[17]. Due to high energy radiation required for this process, the process is very expensive but it can be used to create very straight pores[10].A figure of the process is presented as Figure 1.4a.

1.2.3. Electrospinning

Some polymers, such as polyvinylidene fluoride (PVDF), polyacrylonitrile (PAN), or polystyrene (PS), are electro-spinnable, and hence electrospinning can be an option to produce membranes if these materials are used. The electrospinning process involve applying a high electric field to generate nanofibers from a charged polymer solution or melt[18]. The polymer solution is filled in a syringe, which is placed at a distance from the target plate. The electric field applied stretches the polymer droplets from the tip of the syringe, creating jets of polymeric nanofibers that can be collected at the target. Through further fine-tuning the solution parameters and the electric field, different morphology, and by extension membranes, can be made[10]. A figure of the process in presented in Figure 1.4b.

1.2.4. Sintering

Sintering is a common method for manufacturing not only ceramic membranes, but also polymeric membranes. The process involves first preparing a ceramic/polymer support and a coating solution, which has ceramic or polymer particles, the coating solution is then coated on the support, compressed and heated with the support[19], the spaces between the compressed particles are hence the pores. It is obvious that the particles, i.e. polymers and ceramics, must withstand high pressure and high temperature. This method is mainly used to produce microfiltration membranes[10]. This process is shown as Figure 1.4c.

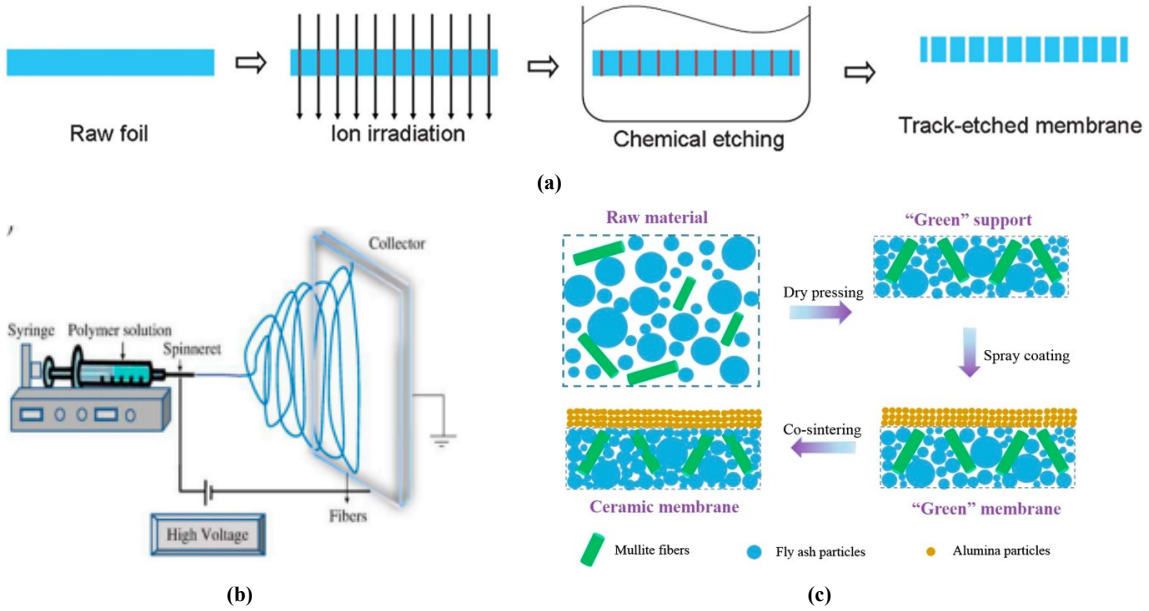

Figure 1.4: Other methods apart from phase inversion methods:(a) A general track etching process for membrane production[20] (b) A typical electrospinning method in vertical setup[21] (c) Sintering manufacturing process of a ceramic membrane[22]

1.3. New methods: 3D printing

Despite numerous conventional techniques used to manufacture membranes, a common downside is that the membrane structure cannot be easily controlled. Pore structure in conventional membranes, including porosity, interconnectivity, distribution, and size, is often asymmetric or unordered[10]. This is because membrane structures are controlled by preparation parameters

such as the sintering temperature[23], bath temperature and duration of irradiation[24]. However, when compared to manufacturing membranes using 3D printing method, the aforementioned methods lack the precise control of pore sizes and membrane structure that the 3D printing methods can provide[10]. If we consider the most common method of manufacturing membranes in the present era is the phase inversion method[11], then there's also an additional downside that toxic solvents required in some membrane manufacturing processes can also cause harm to human workers and the environment[14].

Membrane manufacturing through additive manufacturing is a relatively new field. As of time of writing, the research domain has only started to gain traction in the last 8 years (circa 2014, 2015), with publication numbers rising from less than 10 per year to more than 100 per year[11]. 3D printing of membranes, however, presents the advantages of being able to precisely control the membrane structure during manufacturing[25], and also the characteristic of having low chemical exposure and low amounts of wastes produced[26]. In this section, we outline the various methods that have been used to manufacture membranes. To limit the scope, we will not include the research done on printing membrane spacers, instead we will only focus on those that print the membranes itself directly.

1.3.1. Fused Deposition Modelling (FDM)

Fused Deposition Modelling (FDM), or otherwise know as fused filament fabrication (FFF), is one of the most, if not the most, commonly used 3D printing method[27]. This method works by extruding a filament of melted thermoplastic, depositing them in a layer-by-layer fashion. The extruded material hardens and then the printer proceeds to the next layer[28].

Using the FDM method, Xing et al.[29] reported manufacturing a lotus-leaf inspired membrane. Produced by Poly(lactic acid) (PLA) filaments, the membrane is superhydrophobic and can be further enhanced by chemical etching which decreases the pore sizes and the surface roughness. The final membrane has pore sizes ranging from 40-600μm, which performs a good oil-water separation performance while retaining a high oil flux (using mixture with oil-water volume ratio 1:1). It also has the advantage of low cost, excellent chemical tolerance,and high mechanical durability.

Another research done by Li et al.[30] reported using cellulose acetate (CA), mixed with polyvinyl alcohol (PVA) and silicon dioxide (SiO_2) nanoparticles to print a superhydrophillic and underwater superoleophobic membrane. Cellulose acetate is used due to its low cost, mechanically robust, and chemically versatility. It however has limited hydrophillic properties, so the researchers mixed CA with PVA and SiO_2 nanoparticles to obtain superhydrphillic and underwater superoleophobic properties. The final membrane, with pore sizes ranging from 100-600μm, displayed good mechanical strength and mechanical stability. It also displayed a 99% oil rejection rate (using mixture with oil-water volume ratio 1:1) with anti-oil fouling ability, making it to be easily cleaned and reused after a long period of oil/water separation.

Although FDM being presented as easy to use, cost-effective and straightforward[30], the biggest downside for using FDM for printing membranes is that the resolution of current FDM systems does not allow small pores to be printed. Current commercial systems provide a resolution of around 100μm, so the smallest pores can that can be printed would be larger than 100μm[28]. Al-

though with some post-processing, such as chemical etching[29], smaller pores can be achieved, the printer resolution still provides a large hurdle in how small the pores can be printed. This would cause a problem if less oil or water concentration is in the oil-water mixture, since it would mean that the big pores cannot separate the two liquids as effective as reported.

1.3.2. Selective Laser Sintering(SLS)

Selective Laser Sintering (SLS) systems are powder-based systems, in which successive layers of ceramic or polymeric powder are solidified on top of one another. Laser beams supplying thermal energy fuses the layers of powder together and thus a 3D structure can be obtained by a layer-by-layer fashion[31]. In the case of printing membranes, the laser parameters are varied to obtain optimal results[32].

Yuan et al.[32] reported that by sintering a single thin layer of polyamide powder, the thin layer can be used as a membrane; and by varying three laser parameters: laser power, hatch space (the distance between laser tracks) and the scanning count, membrane characteristics such as porosity and wettability can be optimized or changed. The morphology of the membranes are also influenced by the parameters. Further research by coating candle soot on the membrane makes the membrane superhydrophobic and oleophilic, yet when wetted with water, the property switches making it superoleophobic underwater. The membrane is thus suitable for oil-water seperation[33].

SLS has the advantage of being able to print ceramic membranes, which FDM isn't able to do. There is also no need for post-curing and support structures, which simplifies the printing process[25]. However, laser sintering has been proven to cause rough surfaces, which may be caused by the overheating of the powder[32]. Another downside is that currently there are no research regarding how to control the pore structures and positions directly, empty spaces between fused powder are branded as "pores" yet they are unorganized and hence the membrane performances are harder to optimize[32,33].

1.3.3. Photopolymerization

Resolution is currently the most difficult aspect to overcome when it comes to utilizing 3D printing for manufacturing membranes[11]. Hence, while there are more than enough 3D printing methods on the market and utilized around the world, currently only photopolymerization has been proven to be able to print membranes with small enough pores to be utilized in daily operations such as water filtration[28]. Two photopolymerization methods will be introduced here, namely (1) Stereolithography (SLA) and (2) Digital Light Processing (DLP).

Photopolymerization, as the name suggests, is a broad term that generally refers to the process of curing photo-reactive polymers (otherwise known as photopolymers) with a laser, UV or visible light[28]. In most cases however, photopolymers react to radiation in the UV wavelength[34], so SLA and DLP mostly differ only in the sense of having different projection areas.

In a typical stereolithography (SLA) system, monomers are mixed with light weight photo-intiators to make photopolymers. The photo-initators are excited when exposed to UV light and thus kickstarts the polymerization process, in which monomers are connected and hence the bulk is polymerized[35]. Ceramics can be printed by having suspended powder in the pho-

topolymers[36]. The printing process, similar to that of SLS, is a layer-by-layer process, in which a thin layer of the photopolymer is cured and then another layer is cured either on top or the bottom of it, depending on how the stage moves. A process visualizing this is given as Figure 1.5. Digital light processing (DLP) uses a projector, instead of a light beam, to project the entire target printing area[28], making DLP a faster method but also a less percise method[11].

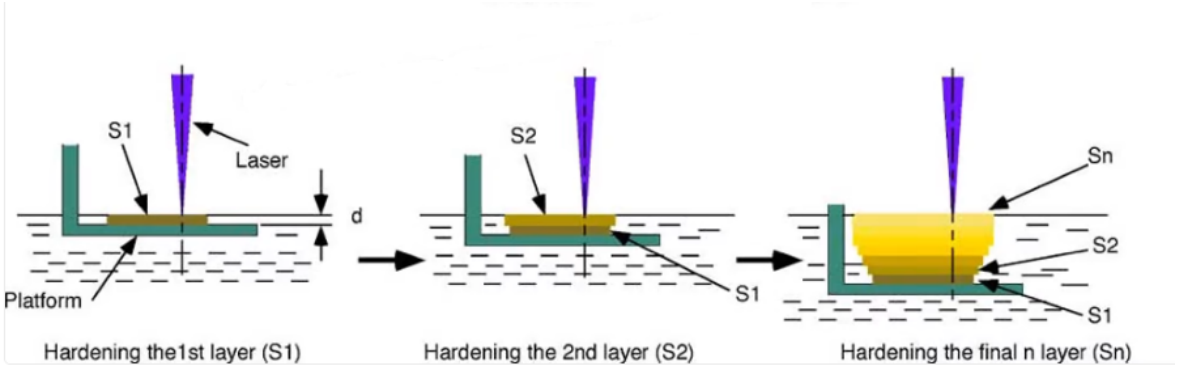

Figure 1.5: Schematic of a typical SLA process[37]

Recent research has shown that indeed both methods can be used to print both ceramic and polymeric membranes, with SLA reported membranes that are suitable for ultrafiltration level membranes, albeit in an uncontrolled way. Mayoussi et al.[38] reported manufacturing a membrane with the SLA method, in which the researchers printed a block with a resin that includes porogen, introducing phase seperation during the photopolymerization process. The porogens seperate with the polymerized parts and creates a web of interconnected holes, which are hence pores, not unlike the pores found in a conventional membrane manufacturing process such as phase inversion. They successfully manufactured a superhydrophobic and superoleophillic membrane with pore sizes ranging from 0.03 to 0.3μm. A simple version of the printing process is provided as Figure 1.6.

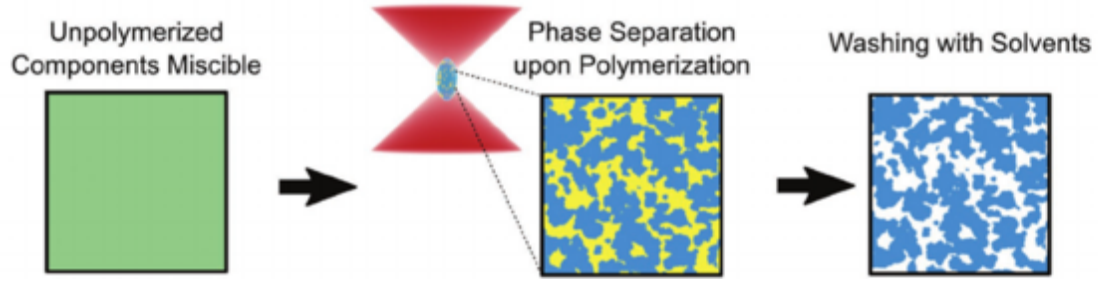

Figure 1.6: SLA process involving phase seperation[39]

Using digital light processing, Jin et al.[40] was able to print ceramic membranes using Al_2O_3 slurry also in a layer-by-layer fashion. After printing, the structures were subjected to high temperature debinding and sintering. Futhermore, a solution of MTMS and MeOH was prepared, the ceramic membrane after sintering was dip-coated with the solution. After dip-coating, a small layer of nanoparticles were formed on the surface of the membranes, enhancing the

oleophillic and hydrophobic properties. The results, with a pore size of 300 μm to 700μm, provided a superhydrophobic membrane with a water contact angle of 162°, the membrane is also mechanically stable and can withstand harsh liquids.

Currently the most commercial photopolymerization methods, which are typically a one photon process, has an inherent resolution limitation due to photopolymerization can happen beyond the focal point, this inherently limits the resolution a so called one-photon polymerization(1PP) can produce[41]. This problem has been partially solved by using a two-photon polymerization process(2PP), in which the initiator in the photopolymer resins has to be initiated by two photons instead of one[42]. Due to 2 photons needed, the light source is normally infrared light, instead of UV light. However, also due to needing 2 photons and the time frame for injecting the second photon extremely small, the process is still extremely inefficient and can hence increase the manufacturing time astronomically[43].

In order to have a higher resolution and also faster printing speed, a photoinhibitor can be added to the photopolymer resin. As the name suggests, a photoinhibitor can inhibit the polymerization, which when excited by the right wavelength, can ”cancel out” the polymerization. This makes the polymerization area smaller than typical 1PP systems, and hence better printing resolution can be performed[41]. A more detailed explanation of the inner workings of such a system, called a dual-wavelength photopolymerization process[44], will be provided in chapter 2. Due to the advantage of having a faster printing time and better printing resolution, it has the advantage of printing microstructures, and thus membranes with microfiltraion purposes, in a reasonable time frame. Yet to the best of the author’s knowledge, this method has yet to be used for printing membranes.

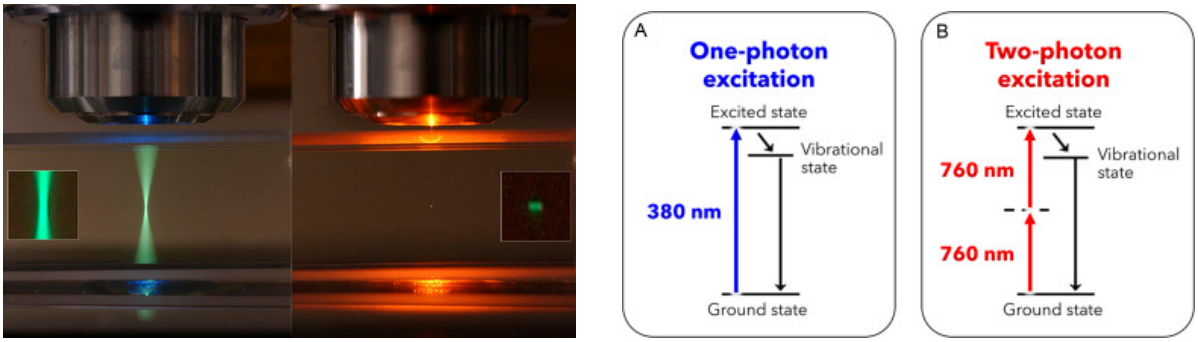

(a) (b)

Figure 1.7: (a) Comparison between a one-photon process and two-photon process respectively, polymerization happens in the green area[45] (b) Comparison between a one-photon process and two-photon process in terms of energy levels and energy wavelengths[46]

1.4. Membrane Characterization

Besides manufacturing, another important aspect for membrane research is characterization. Small changes in the production condition or the geometry of the membranes can affect the final product greatly, changing it’s property and affecting it’s reproducibility[47].Although ”important” membrane parameters are often hard to define, throughout the years of research some parameters have been more widely used and are thus in practice considered the more important parameters to characterize when a new membrane is developed. These parameters are namely

pore geometries (sizes, porosity, distribution...etc.), surface roughness, permeability and rejection rate[48]. Furthermore, membrane characterization can be divided into two different types of parameters, namely ”morphology related parameters” and ”performance related parameters”. The former includes pore geometry and surface roughness, and the latter includes pure water permeability, rejection rate and fouling performance[48,49].

In this research, we will characterize use the following equipments and characterize the following properties:scanning electron microscopy (SEM) will be used to capture basic microfeatures of the membrane. An optical contact angle goniometer will be used to observe the water and n-hexadecane contact angles of the membranes. Atomic force microscopy (AFM) will gives use further insight into the surface roughness of the membrane, and finally, permeability and rejection experiments will be performed in lab-sized equipment, volumetric flow rates will be obtained and then permeability and rejection rates will be calculated.

1.5. Thesis Objective

In this thesis, the main goal is to produce Poly(ethylene glycol) diacrylate (PEGDA) membranes with a pore size of 10μm in diameter through dual-wavelength 3D printing, and fully characterize the membrane and quantify its performance. We then compare this with a commercial hydrophilic PTFE membrane, JCWP14225, which is hydrophilic and has a pore size of 10 μm in diameter. We would like to observe how well or worse the currently researched membrane is compared to commercial ones in order to obtain a direction for further dual-wavelength printed membrane research.

As stated, the final pore size of the membranes is aimed to be in the diameters of 10 μm. The final size of the membrane is 1 x 1 cm^2. This part is done in cooperation with Photosynthetic B.V., located in Amsterdam.

The membranes are then characterized by a few different metrics, namely the pore sizes, pore size distribution, pure water permeability, contact angle, surface roughness, and filtration performance. The commercial JCWP14225 has undergone the same measurements for comparison, the comparison of these membranes will hopefully facilitate directions for further research for 3D-printed membranes via a dual-wavelength system.

References

1. De Haan, A. B., Eral, H. B. & Schuur, B. *Industrial separation processes* (De Gruyter, 2020).
2. Ulbricht, M. Advanced functional polymer membranes. *Polymer* **47,** 2217–2262 (2006).
3. Macedonio, F. & Drioli, E. Membrane engineering for green process engineering. *Engineering* **3,** 290–298 (2017).
4. Xie, W. *et al.* Toward the next generation of sustainable membranes from green chemistry principles. *ACS Sustainable Chemistry & Engineering* **9,** 50–75 (2020).
5. Baker, R. W. *Membrane technology and applications* (John Wiley & Sons, 2012).
6. Cho, H., Yoon, G., Kim, M. & Park, J. Y. Optimal Water Backwashing Condition in Combined Water Treatment of Alumina Microfiltration and PP Beads. *Membranes* **12** (2022).
7. Nunes, S. P. *et al.* Thinking the future of membranes: Perspectives for advanced and new membrane materials and manufacturing processes. *Journal of Membrane Science* **598,** 117761 (2020).
8. Lee, A., Elam, J. W. & Darling, S. B. Membrane materials for water purification: design, development, and application. *Environmental Science: Water Research & Technology* **2,** 17–42 (2016).
9. Norrrahim, M. N. F. *et al.* Emerging Developments Regarding Nanocellulose-Based Membrane Filtration Material against Microbes. *Polymers* **13** (2021).
10. Thiam, B. G., El Magri, A., Vanaei, H. R. & Vaudreuil, S. 3D Printed and Conventional Membranes—A Review. *Polymers* **14,** 1023 (2022).
11. Qian, X. *et al.* A critical review and commentary on recent progress of additive manufacturing and its impact on membrane technology. *Journal of Membrane Science,* 120041 (2021).
12. Dong, X., Al-Jumaily, A. & Escobar, I. C. Investigation of the Use of a Bio-Derived Solvent for Non-Solvent-Induced Phase Separation (NIPS) Fabrication of Polysulfone Membranes. *Membranes* **8** (2018).
13. Figoli, A. in *Encyclopedia of Membranes* (eds Drioli, E. & Giorno, L.) 1–2 (Springer Berlin Heidelberg, Berlin, Heidelberg, 2016).
14. Figoli, A. *et al.* Towards non-toxic solvents for membrane preparation: a review. *Green Chemistry* **16,** 4034–4059 (2014).
15. Gao, J. & Chung, T.-S. Membranes made from nonsolvent-thermally induced phase separation (N-TIPS) for decellularization of blood in dry plasma spot (DPS) applications. *Chemical Engineering Science* **229,** 116010 (2021).
16. Young, D. Etching of radiation damage in lithium fluoride. *Nature* **182** (1958).

17. Apel, P. Y. *et al.* Fabrication of nanopores in polymer foils with surfactant-controlled longitudinal profiles. *Nanotechnology* **18,** 305302 (2007).

18. Tan, X. & Rodrigue, D. A review on porous polymeric membrane preparation. Part I: production techniques with polysulfone and poly (vinylidene fluoride). *Polymers* **11,** 1160 (2019).

19. Zhu, W. *et al.* Integrated preparation of alumina microfiltration membrane with super permeability and high selectivity. *Journal of the European Ceramic Society* **39,** 1316–1323 (2019).

20. Wang, C., Wang, L., Zhu, X., Wang, Y. & Xue, J. Low-voltage electroosmotic pumps fabricated from track-etched polymer membranes. *Lab on a Chip* **12,** 1710–1716 (2012).

21. Mortimer, C. J. & Wright, C. J. The fabrication of iron oxide nanoparticle-nanofiber composites by electrospinning and their applications in tissue engineering. *Biotechnology Journal* **12,** 1600693 (2017).

22. Zou, D., Qiu, M., Chen, X., Drioli, E. & Fan, Y. One step co-sintering process for low-cost fly ash based ceramic microfiltration membrane in oil-in-water emulsion treatment. *Separation and Purification Technology* **210,** 511–520 (2019).

23. Hubadillah, S. K. *et al.* Effect of fabrication parameters on physical properties of metakaolin-based ceramic hollow fibre membrane (CHFM). *Ceramics International* **42,** 15547–15558 (2016).

24. Lalia, B. S., Kochkodan, V., Hashaikeh, R. & Hilal, N. A review on membrane fabrication: Structure, properties and performance relationship. *Desalination* **326,** 77–95 (2013).

25. Dommati, H., Ray, S. S., Wang, J.-C. & Chen, S.-S. A comprehensive review of recent developments in 3D printing technique for ceramic membrane fabrication for water purification. *RSC advances* **9,** 16869–16883 (2019).

26. Yanar, N. *et al.* A New era of water treatment technologies: 3D printing for membranes. *Journal of Industrial and Engineering Chemistry* **91,** 1–14 (2020).

27. Melenka, G. W., Cheung, B. K., Schofield, J. S., Dawson, M. R. & Carey, J. P. Evaluation and prediction of the tensile properties of continuous fiber-reinforced 3D printed structures. *Composite Structures* **153,** 866–875 (2016).

28. Low, Z.-X. *et al.* Perspective on 3D printing of separation membranes and comparison to related unconventional fabrication techniques. *Journal of membrane science* **523,** 596–613 (2017).

29. Xing, R., Huang, R., Qi, W., Su, R. & He, Z. Three-dimensionally printed bioinspired superhydrophobic PLA membrane for oil-water separation. *AIChE Journal* **64,** 3700–3708 (2018).

30. Li, X., Shan, H., Zhang, W. & Li, B. 3D printed robust superhydrophilic and underwater superoleophobic composite membrane for high efficient oil/water separation. *Separation and Purification Technology* **237,** 116324 (2020).

31. Kruth, J.-P., Wang, X., Laoui, T. & Froyen, L. Lasers and materials in selective laser sintering. *Assembly Automation* (2003).

32. Yuan, S., Strobbe, D., Kruth, J.-P., Van Puyvelde, P. & Van der Bruggen, B. Production of polyamide-12 membranes for microfiltration through selective laser sintering. *Journal of membrane science* **525,** 157–162 (2017).

33. Yuan, S. *et al.* 3D printed chemically and mechanically robust membrane by selective laser sintering for separation of oil/water and immiscible organic mixtures. *Chemical Engineering Journal* **385,** 123816 (2020).

34. Gibson, I. *et al. Additive manufacturing technologies* (Springer, 2021).

35. Bártolo, P. J. *Stereolithography: materials, processes and applications* (Springer Science & Business Media, 2011).

36. Wong, K. V. & Hernandez, A. A review of additive manufacturing. *International scholarly research notices* **2012** (2012).

37. All3DP. *Stereolithography / SLA 3D Printing – Simply Explained* `https://all3dp.com/2/stereolithography-3d-printing-simply-explained/` (2022).

38. Mayoussi, F. *et al.* Facile fabrication of micro-/nanostructured, superhydrophobic membranes with adjustable porosity by 3D printing. *Journal of Materials Chemistry A* **9,** 21379–21386 (2021).

39. Mayer, F. *et al.* 3D Two-Photon Microprinting of Nanoporous Architectures. *Advanced Materials* **32,** 2002044 (2020).

40. Jin, Z. *et al.* 3D-printed controllable gradient pore superwetting structures for high temperature efficient oil-water separation. *Journal of Materiomics* **7,** 8–18 (2021).

41. Scott, T. F., Kowalski, B. A., Sullivan, A. C., Bowman, C. N. & McLeod, R. R. Two-color single-photon photoinitiation and photoinhibition for subdiffraction photolithography. *Science* **324,** 913–917 (2009).

42. Van Der Laan, H. L., Burns, M. A. & Scott, T. F. Volumetric photopolymerization confinement through dual-wavelength photoinitiation and photoinhibition. *ACS Macro Letters* **8,** 899–904 (2019).

43. Tromayer, M. *et al.* Wavelength-optimized two-photon polymerization using initiators based on multipolar aminostyryl-1, 3, 5-triazines. *Scientific reports* **8,** 1–11 (2018).

44. De Beer, M. P. *et al.* Rapid, continuous additive manufacturing by volumetric polymerization inhibition patterning. *Science advances* **5,** eaau8723 (2019).

45. Prabhakaran, P. *What is Two-Photon Absorption?* `https://www.l3dw.com/what-is-two-photon-absorption/` (2022).

46. Croissant, J. G. & Durand, J.-O. Mesoporous silica-based nanoparticles for light-actuated biomedical applications via near-infrared two-photon absorption. *The Enzymes* **43,** 67–99 (2018).

47. Reif, O. W. W. in *Sterile Filtration* (ed Jornitz, M. W.) 73–103 (Springer Berlin Heidelberg, Berlin, Heidelberg, 2006). ISBN: 978-3-540-33018-9. `https://doi.org/10.1007/b104245`.

48. Cuperus, F. & Smolders, C. Characterization of UF membranes: membrane characteristics and characterization techniques. *Advances in colloid and interface science* **34,** 135–173 (1991).

49. Singh, R. & Purkait, M. K. in *Membrane separation principles and applications* 111–146 (Elsevier, 2019).

2

Background Knowledge

An introduction to the underlying chemical system and the chemical will be outlined in the first part of this chapter. We will further discuss here how the hardware of the system, i.e. how the 3D printer was designed in previous research and how the system designed by Photosynthetic works in principle.

2.1. A quick glance through photopolymerization

Contemporary commercial photopolymerization mostly utilize UV light as the primary initiating source[1]. The process is visualized in Figure 2.1a. In this reaction, monomers are mixed with photoinitiators to create photopolymers. For some photopolymers the addition of co-initiators is also needed, it is a separate compound that does not absorb light but interacts with an activated photoinitiator to produce radicals[2]. The photopolymerization reaction consists of mainly three steps: initiation, propagation, and termination. In the initiation step, radicals are formed when photoinitiators are exposed under UV light, either with or without the help of co-initiators; the radicals are then connected with monomers to form a so called ”radical center”, which kickstarts the polymerization process. The radical centers then connect with other monomer molecules, this is the propagation step. Finally, there are mainly two ways of termination, either the radical centers connect with one another, dubbed ”bimolecular termination”, or the photoinitiators are depleted and thus no more initiation can happen, called ” primary depletion”. As the name suggests, the main termination method is through depleting the photoinitiators[3]. Figure 2.1a explains this process in a more visual way. This single-wavelength photopolymerization process has a significant downside, in which the process is hard to contain and can cause over-curing in unwanted areas[4,5].

To solve this problem, dual-wavelength photopolymerization has been developed and reported by various research groups[5–7]. As shown in Figure 2.1b, when compared to the typical photopolymerization process, a photoinhibitor is also included. The photopolymerization process is initiated by blue light and inhibited by UV light, instead of initiated by UV light. Similar to that of the UV polymerization, the photoinitiators are excited by blue light to an excited state, and with the help (or without) of co-initiators, radicals can be produce and kickstart the polymerization process. On the other hand, when the photopolymer is under UV light, another reaction would happen, the photoinhibitor would react and create a larger amount of inhibition

radicals and less initiation radicals[8]. The inhibition radicals could then stop the polymerization process combining with the radicals[5].

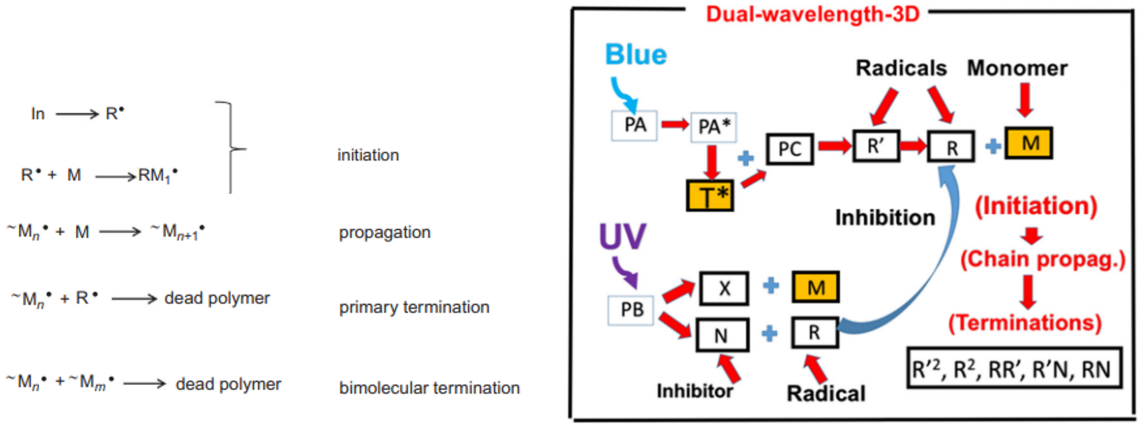

(a) (b)

Figure 2.1: (a) Process of UV polymerization, radicals(**R**·) are created from photoinitiators(**In**) thorugh absorbing UV light, the radicals then combine with monomers(**M**) to initiate polymerization[3]. The picture doesn't include a co-initiator. (b) Process of dual-wavelength polymerization, the photoinitiators(**PA**) are excited by blue light, combining with co-initiators(**PC**), radicals(**R**) can be produced and polymerization can be kick-started. UV light will create inhibitor radicals(**N**) and some initiator radicals(**X**, for showing difference), the inhibitors will combine with radicals and stop the polymerization process[5]

The advantage of such a system is that, as previously argued, the dual-wavelength system can confine the polymerization better when compared to a UV single wavelength system[9], while at the same time having a much shorter manufacturing time (minutes compared to days) when compared to a 2PP system[10].

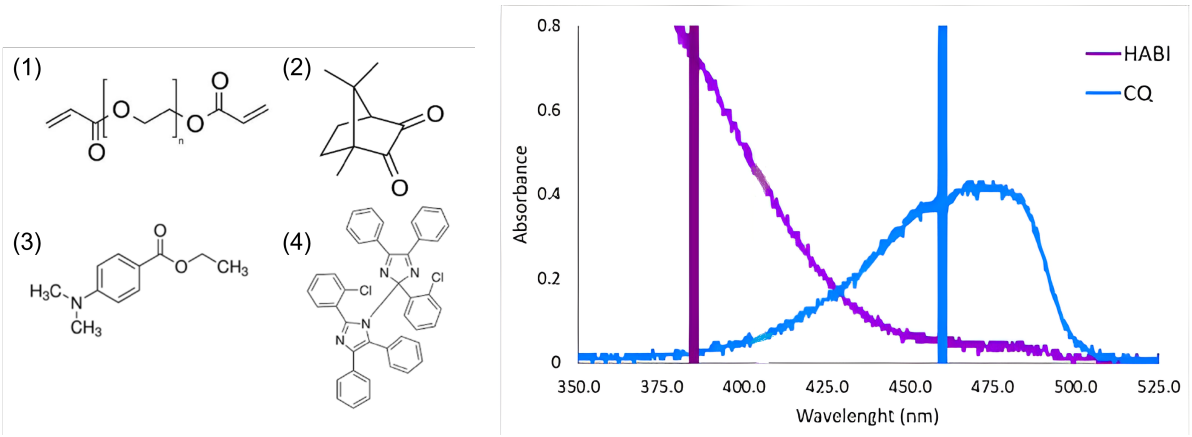

(a) (b)

Figure 2.2: (a) The chemical structures of chemicals used in the photopolymer resin[7]: (1) monomer PEGDA (2) photoinitiator CQ (3) co-initiator EDAB and (4) photoinhibitor o-Cl-HABI (b)The absorbance spectrum of CQ and HABI, wavelengths of 380 and 460 nm are also marked.

In our system, the specific chemicals used are as the following: camphorquinone (CQ), ethyl 4-(dimethylamino)benzoate (EDAB), bis[2-(ochlorophenyl)-4,5-diphenylimidazole] (o-Cl-HABI)

and Poly(ethylene glycol) diacrylate (PEGDA). As photoinitiator, co-initiator, photoinhibitor and monomer, respectively. Their chemical structures are shown as Figure 2.2a. The chemicals are well-mixed as a photopolymer resin. PEGDA is selected due to it's oleophobic and hydrophillic property[11], while EDAB is a commomly used co-initiator that has been proven to work reliably[12]. The wavelengths used in our system are 460 nm and 380 nm for blue light and (near) UV light, respectively. As shown in Figure 2.2b , CQ absorbs light strongly at a wavelength of 460 nm while o-Cl-HABI has the same absorbance as CQ at around 380 nm. As one can observe from Figure 2.2b, CQ and HABI has not much overlap in these two wavelengths, resulting in when the resin is shined in blue light, photopolymerization can happen while when the resin is shined in (near) UV light, photoinhibition can happen[7]. To put it simply, by adjusting the projection area of UV light and blue light, one could create geometries that have areas that are polymerized and not polymerized, one could also change the polymerization level, or more appropriately know as conversion[13], with changing the ratio of UV light and blue light shined to a given area.

2.2. Dual-Wavelength 3D Printing System

A dual-wavelength printing system, as the name suggests, utilizes two wavelengths, the chemicals have been introduced in the previous section, and both UV and blue light are utilized for inhibition and initiation, respectively. Researchers Harry van de Laan and Martin de Beer and their respective teams have developed their own dual-wavelength 3D printing systems, the former utilizes only the basics of photoinitiation and photoinhibition, with shining UV to only unwanted areas and blue light for polymerization target areas[8], shown in Figure 2.3a. De Beer et al. improved on this idea with incorporating a long pass diachroic mirror, it can more project more complicated structures through this setup[7,14], as shown in Figure 2.3b.

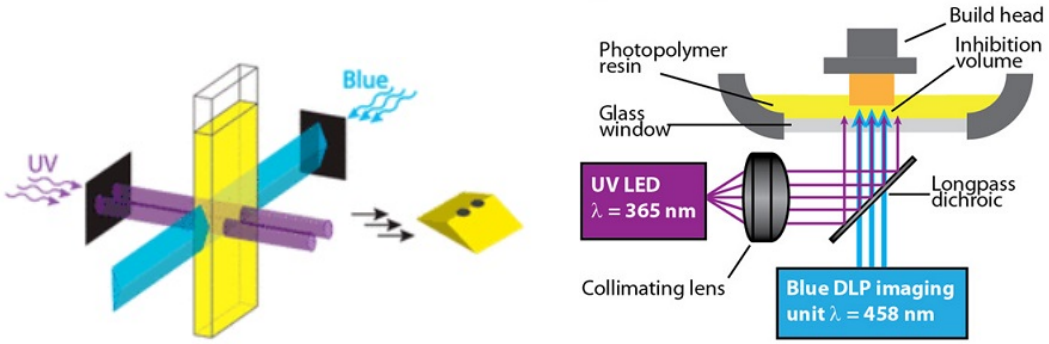

Figure 2.3: (a) The 3D printing system developed by Dr. Harry van de Laan[8] (b) The 3D printing system, incorporating a long pass diachroic mirror, developed by Dr. Martin de Beer[7,14]

The system we utilized for our research has been designed and patented by Photosynthetic B.V.[15,16]. The system utilizes a DLP unit to produce the initiation and inhibition wavelengths, it is visualized as Figure 2.4. The printing x-y resolution is further determined by the microscope lens as shown in the system. The microscope lens collects the light and projects it into the resin. As a microscope works in reverse order, the projected image is then minimized into a smaller projection image on the resin, this serves as the basis of the printing process, This also gives

the printer resolution as the following:

$$R_{xy}(\mu m) = 14/M \tag{2.1}$$

In which R_{xy} is the resolution in the x-y plane, and M is the magnification of the microscope lens. Throughout this research, the M is chosen as 10x, which gives a resolution of 1.4 μm. However, to print smaller features and by extension, smaller pores, a 20x magnification lens might be needed as it creates a smaller projection area on the resin.

The UV and Blue light are projected in a layer-by-layer fashion, yet in extremely short sequences (timescales in milliseconds). At the same time, the lenses move slightly downwards, making the printing process more akin to printing a bulk volume. In other words, a volume, instead of a very thin layer, can be printed in a very short time. The target is thus printed in a volume-by-volume fashion, instead of a layer-by-layer fashion. In our application, what this essentially means is that instead of printing a thin layer of the whole membrane, we print a small tile of the membrane, and then ”stitch” the tiles into one larger volume of a membrane. A visualization picture of the printer has been provided as Figure 2.4.

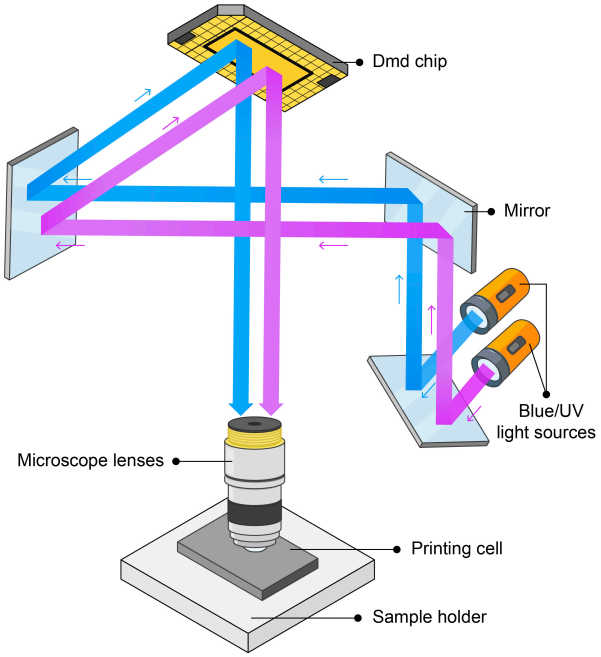

Figure 2.4: Simplified visualisation of the 3D printer and its process, the microscope lenses move downwards when printing a tile and then resets when a tile is finished printing. The sample holder then moves for the next tile to be printed.

References

1. Gibson, I. *et al. Additive manufacturing technologies* (Springer, 2021).
2. Stansbury, J. W. Curing dental resins and composites by photopolymerization. *Journal of esthetic and restorative dentistry* **12,** 300–308 (2000).
3. Andrzejewska, E. in *Three-Dimensional Microfabrication Using Two-Photon Polymerization* Second Edition, 77–99 (William Andrew Publishing, 2020).
4. Gao, W. *et al.* The status, challenges, and future of additive manufacturing in engineering. *Computer-Aided Design* **69,** 65–89 (2015).
5. Lin, J.-T., Cheng, D.-C., Chen, K.-T. & Liu, H.-W. Dual-wavelength (UV and blue) controlled photopolymerization confinement for 3D-printing: Modeling and analysis of measurements. *Polymers* **11,** 1819 (2019).
6. Scott, T. F., Kowalski, B. A., Sullivan, A. C., Bowman, C. N. & McLeod, R. R. Two-color single-photon photoinitiation and photoinhibition for subdiffraction photolithography. *Science* **324,** 913–917 (2009).
7. De Beer, M. P. *et al.* Rapid, continuous additive manufacturing by volumetric polymerization inhibition patterning. *Science advances* **5,** eaau8723 (2019).
8. Van Der Laan, H. L., Burns, M. A. & Scott, T. F. Volumetric photopolymerization confinement through dual-wavelength photoinitiation and photoinhibition. *ACS Macro Letters* **8,** 899–904 (2019).
9. Lin, J.-T., Liu, H.-W., Chiu, Y.-C., Chen, K.-T. & Cheng, D.-C. 3-Wavelength (UV, Blue, Red) Controlled Photo-Confinement for 3D-Printing: Kinetics and Modeling. *IEEE Access* **8,** 49353–49362 (2020).
10. Weisgrab, G. *et al.* 3D Printing of large-scale and highly porous biodegradable tissue engineering scaffolds from poly (trimethylene-carbonate) using two-photon-polymerization. *Biofabrication* **12,** 045036 (2020).
11. Wang, Y. & Gong, X. Special oleophobic and hydrophilic surfaces: approaches, mechanisms, and applications. *Journal of Materials Chemistry A* **5,** 3759–3773 (2017).
12. Kowalska, A., Sokolowski, J. & Bociong, K. The photoinitiators used in resin based dental composite—a review and future perspectives. *Polymers* **13,** 470 (2021).
13. Kricheldorf, H. R., Scheliga, F. & Weidner, S. M. What does conversion mean in polymer science? *Macromolecular Chemistry and Physics* **222,** 2100010 (2021).
14. Scott, T. *et al. Polymerization photoinhibitor* 2022. `https://patentimages.storage.googleapis.com/59/a1/c0/693ba700a5a2eb/US20220106417A1.pdf`.
15. Kostenko, A. *Confocal lithography* 2019. `https://patentimages.storage.googleapis.com/f0/2e/a2/0bd6a2f3b4c2bd/NL2024460B1.pdf`.

16. Kostenko, A. *Controlled polymerization of a target zone in a photopolymerizable medium* 2020. https://patentimages.storage.googleapis.com/95/41/5b/36cdbe51faf775/WO2020064779A1.pdf.

3

Methods and Materials

3.1. Materials

The photopolymer resin for this study was prepared using commercially available materials. Camphorquinone (CQ), ethyl 4-(dimethylamino)benzoate (EDAB), and 2,2'-bis (2-chlorophenyl)-4,4',5,5'-tetraphenyl-1,2'-biimidazole (o-Cl-HABI) are used as photoinitiator, co-initiator, and photoinhibitor respectively. Poly(ethylene glycol) diacrylate (700) (PEGDA, molecular weight = 700g/mol) is used as monomer in respective printing experiments.

Other chemicals used during this research are the following: Ethanol is used as a cleaning solvent. Isopropanol (IPA) and methyl isobutyl kentone (MIBK) are used as the post-printing solvent to wash away residual resin. N-hexadecane is used for contact angle measurements and filtration experiments. sodium dodecyl sulfate (SDS, Sigma-Aldrich, USA) and oil red EGN are used for emulsion manufacturing in filtration experiments measurements. All of the chemicals used were purchased from Sigma-Aldrich, The USA.

3.2. Designing a membrane

As previously discussed, the printer prints in a volume-by-volume, or tile-by-tile fashion, meaning we design the individual tile, and then the printer repeats every tile until we reach the desired tile number. The number of pores, pore diameter, and thickness of a tile of the membrane were manually decided beforehand. The respective parameters are 256 pores (16 pores in x and y directions, respectively), 10 um in diameter, and 70 um in thickness. According to these parameters, a target model of the membrane was then produced. The target is shown as Figure 3.1. The target depicts the desired conversion rate at every pixel of the membrane.

The light projection was calculated via an iterative procedure using the gradient descent method. UV and blue light projection at every pixel is calculated by considering the point spread function (psf), which is a function of numerical aperture (NA) and wavelength (λ)[1]. The UV and blue light intensities projected on the resin are corrected by convoluting the psf and the rate of polymerization is then derived from the following equation[2]:

$$R_{poly} = k(I_{blue,pixel} - \beta I_{UV,pixel})^{0.5} \tag{3.1}$$

In which R_{poly} is the polymerization reaction rate. k is the reaction rate constant, β is the inhibition coefficient, I_{blue} and I_{UV} are the blue light and UV light intensities, respectively.

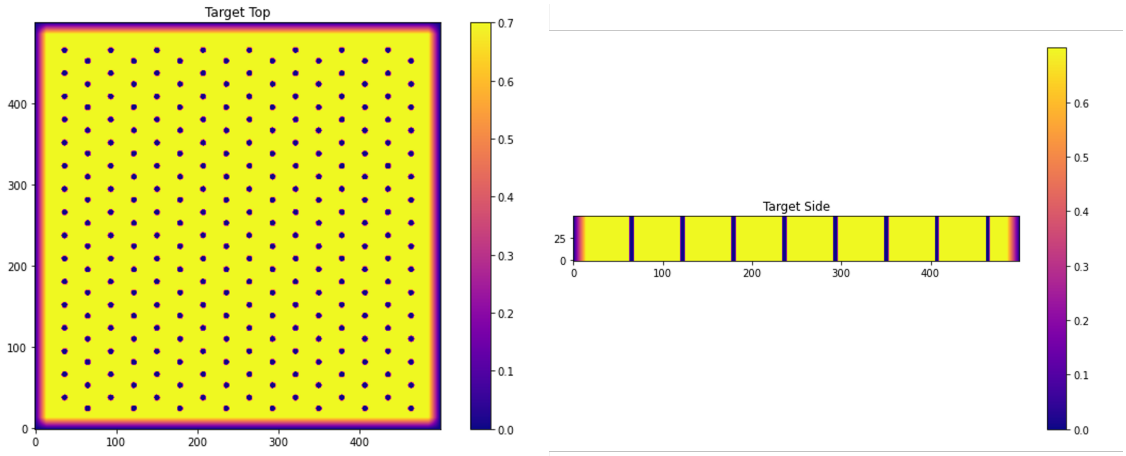

Figure 3.1: Target of the designed membrane, the right-hand bar indicates conversion(%)/ The x, y and z values are number of pixels.

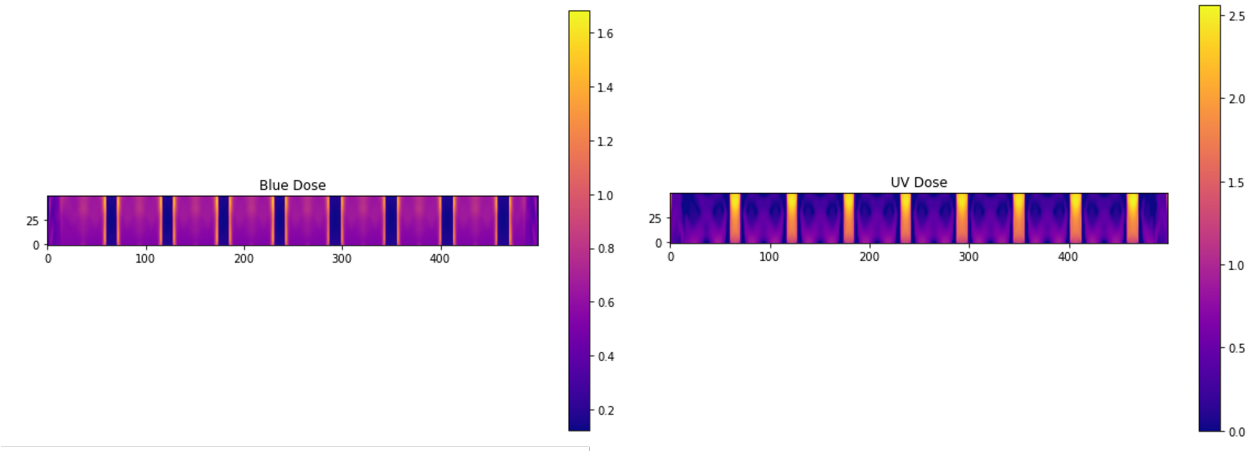

Figure 3.2: The dosage required for printing the membrane. The right-hand bar depicts the time amount in which the respective light source is used. The unit is in seconds (s). The x and z values are the number of pixels.

The reaction rate constants k and β are measured beforehand. The conversion is calculated via the polymerization reaction rate via the following equation[3]:

$$C_{xyz} = \int R_{poly} dt \tag{3.2}$$

In which C_{xyz} is the conversion of a certain pixel. The conversion is then compared with the target, providing a mean square error term. Via the gradient descent method, a new set of light projections can be determined[4]. The algorithm reaches a solution once the mean square error is minimized. This produced the printing model, with the information on the actual light dosages required and the chemical conversion at each location. The light intensities are shown as Figure 3.2, and the chemical conversion is shown as Figure 3.3. A flowchart of the procedure is also provided as Figure 3.4. A more detailed version of the calculation method is provided by Mulder et al[5]. and Kotsenko et al[6].

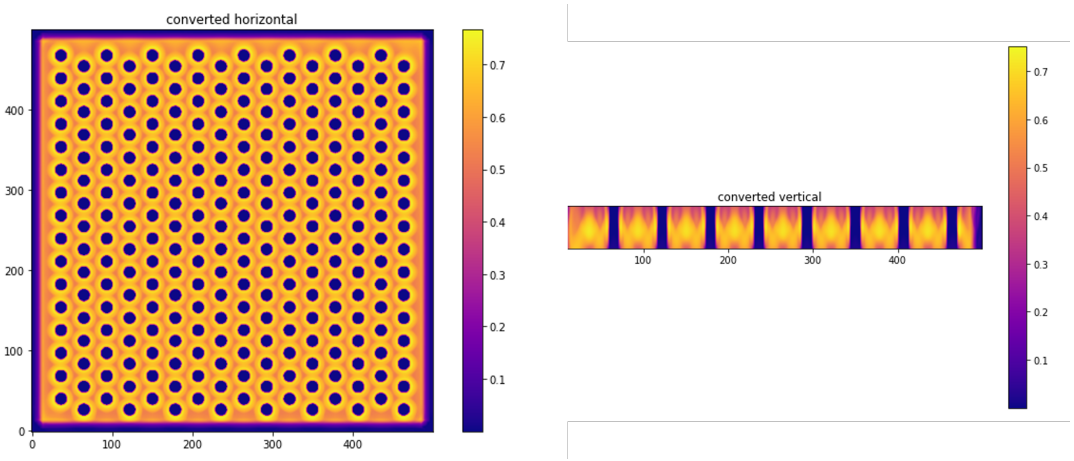

Figure 3.3: The final calculated conversion of the membrane, indicating the conversion rate of every pixel of the membrane, and the right-hand bar indicates conversion(%). The x, y, and z values are the number of pixels.

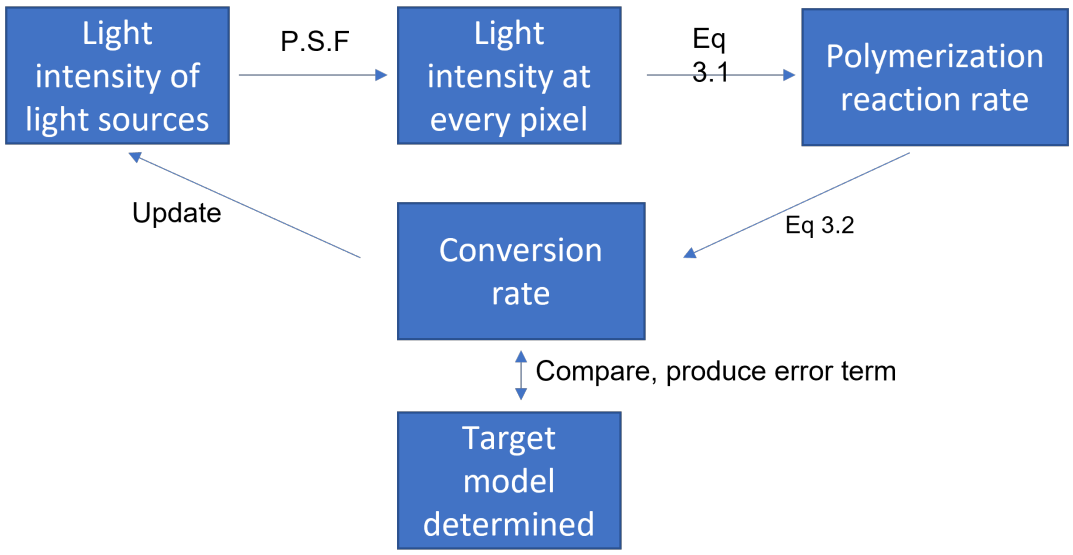

Figure 3.4: A flowchart of the procedure of how the designed membrane is calculated

3.3. Printing a membrane

The general process of producing a membrane is described in this section. Specific reasons for steps will also be explained, as during the research process these were specific steps that caused difficulties in repeatability.

First, the photopolymer resin was produced via mixing CQ, EDAB and HABI with PEGDA. The resin was then used to fill the printing cell. The printing cell was fabricated via the following procedure:
1. Micro cover glasses (24x24 mm^2, Brand, Germany) and microscope glasses(76x26 mm^2, Brand, Germany) were first cleaned with ethanol and then air-dried via a lab-sized high-pressure blower.
2. A small portion of the aforementioned resin was mixed with spacer beads of 70 μm (Micropearl SP series, Sekisui Chemical Co., Ltd, Japan) with a concentration of 0.0033 g/1 ml. 4 dots of 10 μl of the mixed resin are then dotted on the four corners of the micro cover glass.
3. The cover glass was first covered on the top of the mixed resin, 50 μl of resin was then further supplied from the side, using a pipette, to the space between the top and bottom glass. This produced a printing cell with particles on the four corners of the printing zone. The top and side view of said printing cell are provided as Figure 3.5.

This cell design and the filling procedure has been found to guarantee a reproducible thickness of 70 μm, since it eliminates the possibility of thickness variation of the membrane, which can be caused by not fully filling the resin or a collapse of the top cover glass.

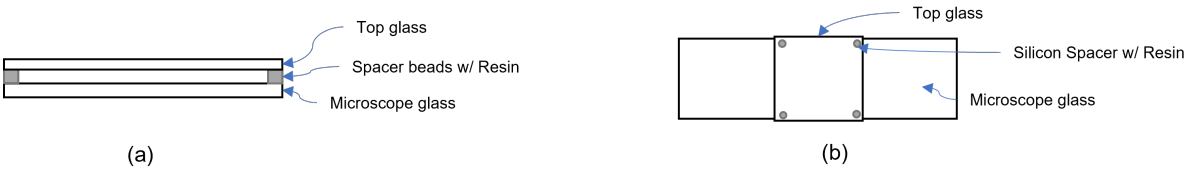

Figure 3.5: (a) The side view of the cell (b) The top view of the cell

The printing cell is then set on the sample stage and printing can be started. The calculated model discussed in the previous section is then read by the printer and settings are adjusted accordingly. After this, the printing procedure starts.The membrane was printed in a layer-by-layer and tile-by-tile fashion. Each tile is printed layer-by-layer over a time span of 5 s. To reach a membrane size of 1*1 cm^2, we print 256 tiles, 16 tiles in the x and y directions, respectively.

The tiles are automatically stitched together by the polymerized resin on the edges of every tile. The printing process started at the bottom of the filled resin (top of the bottom glass), where the lens focus is. When printing starts, the lenses move upwards whilst projecting light in a blue-UV-blue-UV sequence. After finishing one tile the lens reset to its original position, i.e. the focus plane at the top of the bottom glass, and the sample stage moves to the next position, printing another tile. The printing stops when the desired sample size is met and the sample can then be taken out. The process is visually explained in Figure 3.6. Note at the start of the printing process, the tiling sequence is a bit different, to prevent the top glass from collapsing, resulting in a thinner membrane at one side then the other, the four corners and the

middle tile of the membrane were first printed, as shown in Figure 3.7. The full membrane was then printed in sequence.

Finally, the printed product is taken out and washed under a mixed solvent of isopropanol and methyl isobutyl ketone (MIBK), this procedure is done so that unpolymerized resin can be washed away[7], which would be the case of resin in the pores for our samples. The post-processed sample was then heated at a temperature of 160 °C for a duration of 20 min. This increases the cross-linking density and thus the storage modulus of the monomer, increasing the mechanical strength of the final membrane[8]. To prevent local swelling from creating cracks in the membrane[9], the product was preserved in a small bottle filled with water. The membranes were left for 2-3 days in water before further testing.

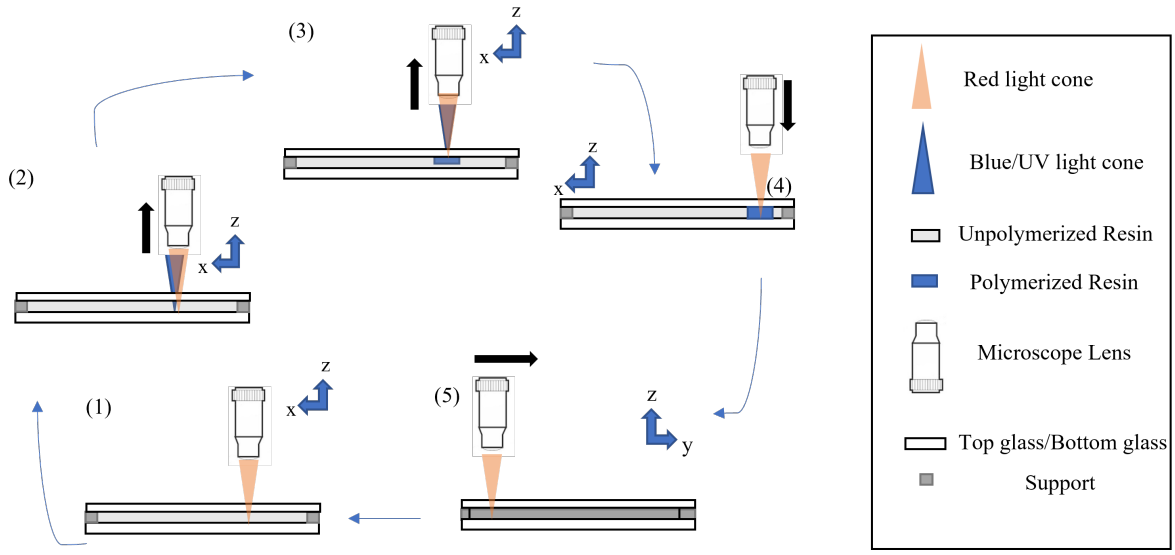

Figure 3.6: Process of printing is visualized, red light is also used in the printing process but doesn't effect the resin, as shown by De Beer et al[7]. A camera is used to see the area, which is mainly illuminated by red light. The steps of the printing process: (1) The lenses are focused on the bottom of the top glass, using red light we can focus (2) The UV/Blue light starts flashing while the lenses start moving downwards (3) A small volume of the resin is cured (4) The lenses move back to focus on bottom of top glass (5) The lenses move to location for next designated tile, repeat till wanted structure is printed.

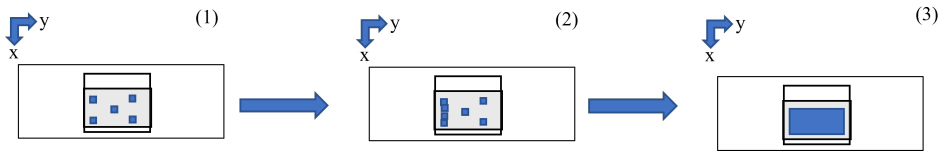

Figure 3.7: Illustration of the printing scheme. (1) The First four corners were first printed, (2) The y direction is then printed, slowly filling the space in between, (3) The membrane is printed.

3.4. Microscopy imaging

The samples were cut into smaller pieces using liquid nitrogen. The samples were dipped into liquid nitrogen and then separated into smaller pieces for observation and imaging with scanning electron microscopy (SEM) (JSM-6010LA, JEOL, Japan). The acceleration voltage

is 10kV or 15kV. All samples were coated with gold with a sputter coater(JFC-1300, JEOL, Japan) with a current of 20mA and 30 secs.

To further investigate the roughness of the printed membranes, atomic force microscopy (AFM) (Dimension Edge, Bruker, USA) was also employed to measure the root mean square roughness of the printed membrane in tapping mode.

To observe the membrane in-situ during experiments, we have also utilized an optical microscopy (Navitar 12x, Darwin Microfluidics, France) coupled with a microscopy camera (USB 3.0. Pixelink, Canada) to capture membrane deformation during the experiments.

3.5. Pore size distribution

The pore size distribution was collected via the image processing program ImageJ and further analyzed via a self-made Matlab code[10,11].

SEM photos of the membrane were first input into the imageJ program. The pore areas were then calculated via the analyze particle function. The diameter can then be calculated. The final pore size distribution was then organized and obtained. The procedure is shown more clearly in section A.2 and section A.3.

3.6. Contact angle(CA) measurement

The contact angles of air and n-hexadecane in water, also the contact angles of water and n-hexadecane in air, were measured. Both static and dynamic contact angle measurements were measured in all cases with an optical contact angle measuring system (OCA) (OCA 25, dataphysics).

All static contact angle measurements were performed using a 6 μl droplet. The water-in-air and oil-in-air experiments were performed using the sessile droplet method, with water and n-hexadecane respectively. The underwater experiments were performed using the captive bubble method, with a 6μl droplet of either air or n-hexadecane.

Dynamic contact angle measurements were performed in a similar manner. First, a 2 μl of the droplet is dropped on the surface of the membrane, the needle was then submerged into the droplet. Then an advancing and receding contact angle (ARCA) setting was set with a dosage of 6 μl and a speed of 0.5 μl/s for 6 cycles, with 6 s of advancing, 2 s of pause, and 6 s of receding. The contact angles were detected automatically and recorded.

3.7. Permeability measurement

The permeability of the membranes was measured via a dead-end volumetric flow rate measurement. The membranes were placed in a self-designed dead-end membrane cell and pressure was increased step-wise from 100 to 500 mbar with increments of 100 mbar. The permeating flow rate was measured simultaneously using a flow sensor (flow sensor premium BSF1, Elveflow, France). A simplified view of the self-designed setup is shown as in Figure 3.8.

The permeability of the membrane was calculated via Darcy's law[12]:

$$Q = \frac{\kappa A}{\mu}\frac{\Delta p}{h} \tag{3.3}$$

in which Q is the volumetric flow rate(μl/min), κ is the permeability, A is the membrane cross-section area (m^2), μ is the dynamic viscosity (Pa*s), Δp is the pressure drop (mbar) across the membrane and h is the membrane thickness(m).

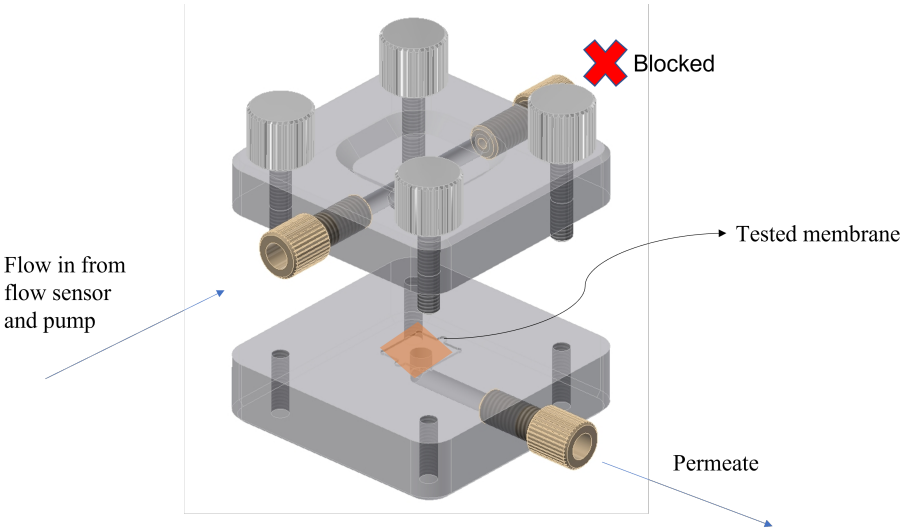

Figure 3.8: The side view of the self-designed and manufactured dead-end cell. The depth of the membrane seat is 70 μm (the same as membrane thickness).

3.8. Separation Performance measurement

Separation performance of membranes was investigated via filtration of oil-in-water emulsions. We utilized two methods to make the emulsion. The first method works as a proof of concept, in which the emulsion is a modified version of the emulsion provided by Li et al[13] and the second method is a standard oil-in-water emulsion produced via the method provided by Dickhout et al[14]. We call the first one the "proof of concept (POC) emulsion" and the second one the "standard emulsion".

The POC emulsion was manufactured by mixing sodium dodecyl sulfate, n-hexadecane, demineralized water, and oil red EGN. 460 mg of SDS was mixed with 1 liter of demineralized water (1.6 x 10^{-3} M) at 14000rpm with the Ultra-Turrax T18 mixer (IKA, the Netherlands) for 2 minutes. To measure the filtration performance, red EGN was separately added to n-hexadecane and filtered, 40 ml of n-hexadecane and 40 ml of water is then mixed together and sonicated for 30 mins to create an emulsion. The oil-red EGN is needed for absorbance measurement in a uv-vis spectrofotometer (DR6000, HACH, The USA). We use this to determine the filtration performance. Further explanation is given in section A.4. Due to phase separation into oil-rich and water-rich regions, the feed for separation performance experiments we use here is the water-rich region, as shown in Figure 3.9.

The standard oil-in-water emulsion was again manufactured by first making a 1.6 x 10^{-3} M SDS solution. We mixed 460 mg of SDS with 1 liter of demineralized water at 14000rpm with

the Ultra-Turrax T18 mixer. 600 mg of n-hexadecane was then injected with a syringe close to the mixer head and mixed for 10 minutes to generate the oil-in-water emulsion. Finally, 0.04g of oil red EGN is mixed with the emulsion for another 2 minutes. The emulsion has a final n-hexadecane concentration of 600 mg/L. The droplet size of both emulsions was measured via a particle size analyzer (Mastersizer 3000, Malvern Panalytical, the UK). The POC emulsion has a wide range of particles from circa 1 μm to 200μm, with an average of around 54 μm. The standard emulsion has particles of about 1 to 20μm, with an average of 3.44 μm, as provided in Figure 3.10.

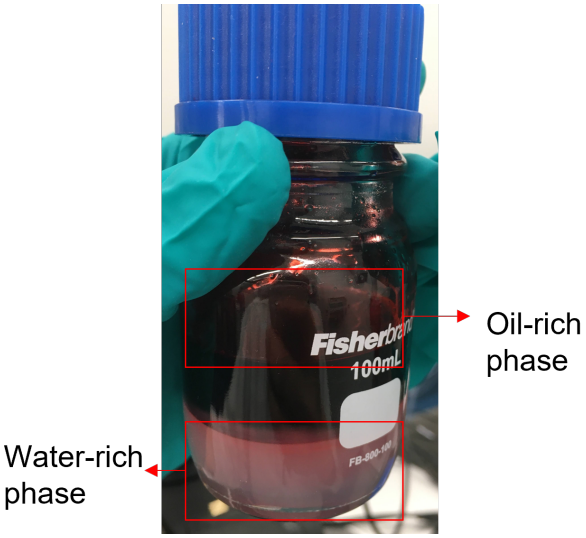

Figure 3.9: The POC emulsion, the water-rich phase is used as feed for separation experiments.

To measure the rejection ratio, the absorbance of the feed and flux were measured, and the rejection ratio is then calculated with the following equation:

$$R(\%) = 1 - \frac{C_p}{C_f} x100 \tag{3.4}$$

In which C_p and C_f (mg/L) are the concentration of the oil in the permeate and feed solutions, respectively.

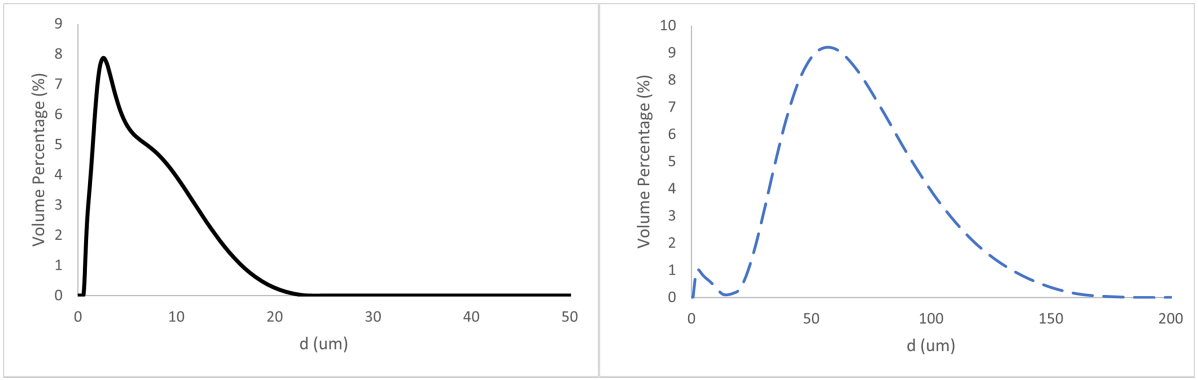

Figure 3.10: The droplet size distributions of (a) The standard emulsion and (b) The POC emulsion

References

1. Schroeder, D. J. *Astronomical optics* (Elsevier, 1999).
2. Van Der Laan, H. L., Burns, M. A. & Scott, T. F. Volumetric photopolymerization confinement through dual-wavelength photoinitiation and photoinhibition. *ACS Macro Letters* **8,** 899–904 (2019).
3. Achilias, D. S. & Siafaka, P. I. Polymerization kinetics of poly (2-hydroxyethyl methacrylate) hydrogels and nanocomposite materials. *Processes* **5,** 21 (2017).
4. Bottou, L. in *Neural networks: Tricks of the trade* 421–436 (Springer, 2012).
5. Mulder, D.-J., Van Vliet, W., Laagland, M., Narayanan, A. & Kostenko, A. *Rapid microprototyping by single-photon two-wavelength volumetric lithography* in *Photonics West* (2023).
6. Kostenko, A. & Narayanan, A. *Multi-wavelength volumetric lithography* in *Advanced Fabrication Technologies for Micro/Nano Optics and Photonics XV* (2022), PC120120I.
7. De Beer, M. P. *et al.* Rapid, continuous additive manufacturing by volumetric polymerization inhibition patterning. *Science advances* **5,** eaau8723 (2019).
8. Sung, J., Lee, D. G., Lee, S., Park, J. & Jung, H. W. Crosslinking dynamics and gelation characteristics of photo-and thermally polymerized poly (ethylene glycol) hydrogels. *Materials* **13,** 3277 (2020).
9. Li, X. *et al.* 3D printing of flexible liquid sensor based on swelling behavior of hydrogel with carbon nanotubes. *Advanced Materials Technologies* **4,** 1800476 (2019).
10. Arganda-Carreras, I. *et al.* Trainable Weka Segmentation: a machine learning tool for microscopy pixel classification. *Bioinformatics* **33,** 2424–2426 (2017).
11. MathWorks, I. *MATLAB 2017b* 2017.
12. Darcy, H. *Les fontaines publiques de la ville de Dijon* (V. Dalmont, 1856).
13. Li, X., Shan, H., Zhang, W. & Li, B. 3D printed robust superhydrophilic and underwater superoleophobic composite membrane for high efficient oil/water separation. *Separation and Purification Technology* **237,** 116324 (2020).
14. Dickhout, J. M., Kleijn, J. M., Lammertink, R. G. & De Vos, W. M. Adhesion of emulsified oil droplets to hydrophilic and hydrophobic surfaces–effect of surfactant charge, surfactant concentration and ionic strength. *Soft Matter* **14,** 5452–5460 (2018).

4

Results and Discussion

4.1. 3D printing of membranes

The manufactured membrane has, as previously mentioned, a porosity of 5%, pore diameter of 10 μm, and thickness of 70 μm. The total sample length and width are 1 cm by 1 cm.

The top, bottom, and side view of the membrane are provided as Figure 4.1. The top and bottom are defined as the same as in the cell. So the bottom is first printed and moved through to the top. From the figure, the membrane has a uniform pore distribution with 256 pores on every tile. The pores are also straight from top to bottom. Curiously, when observed from the side, there are small ripples on the surface. We theorize this to be caused by small air bubbles either already in the cell or sucked in due to volume shrinkage[1] of the printed tiles. These trapped air bubbles block polymerization at the very end of the printing process (the top of the membrane), causing a small thickness not to be polymerized. Fortunately, this effect did not cause any changes to the membrane porosity or the printing process.

The membrane pore size distribution is measured via ImageJ. The obtained distribution (Figure 4.2) shows that the membrane has a very narrow pore size distribution (from 6.1 - 7.4 μm). It further demonstrated that the final pore radius of the printed membrane is smaller than the designed value of 10 μm, with a 30% decrease in pore size.. This was likely due to the fact that the precision of the projected area was still not precise enough and can cause over-polymerization at the edge of the pore, which resulted in a smaller pore radius than designed.

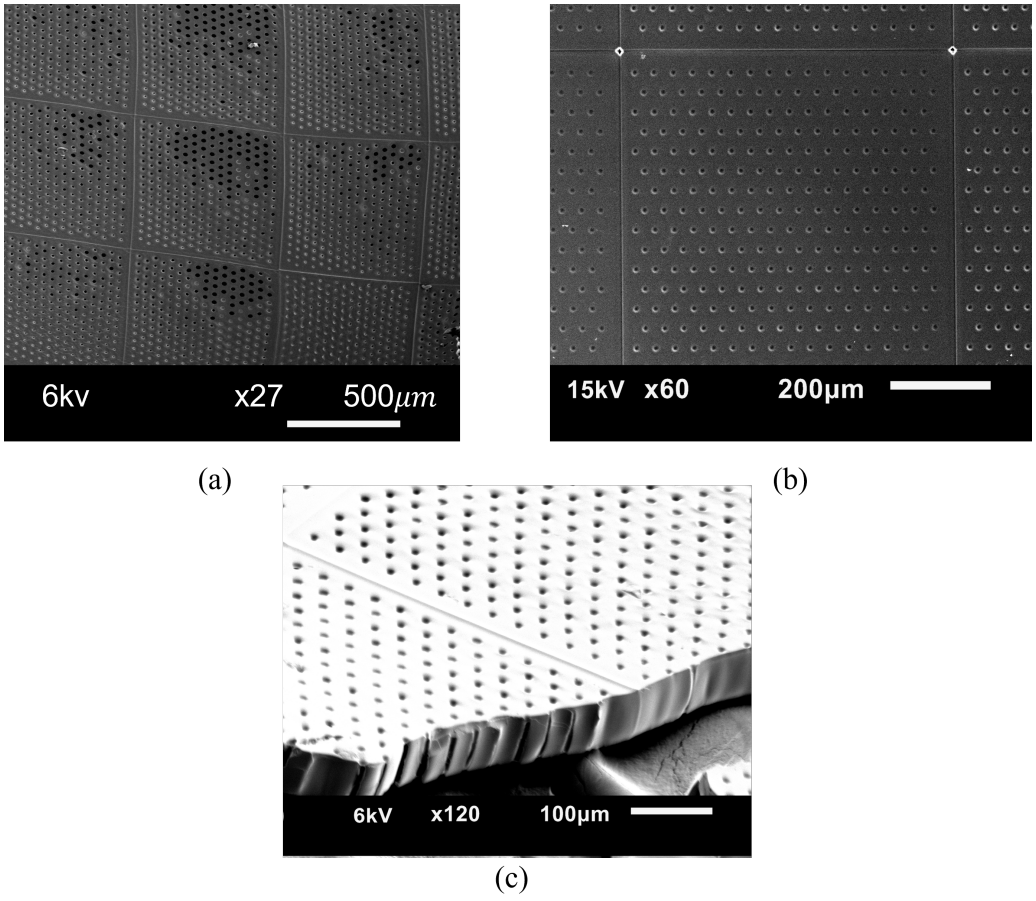

Figure 4.1: (a) The top view of the membrane (b) The bottom view of the membrane (c) The side view of the membrane

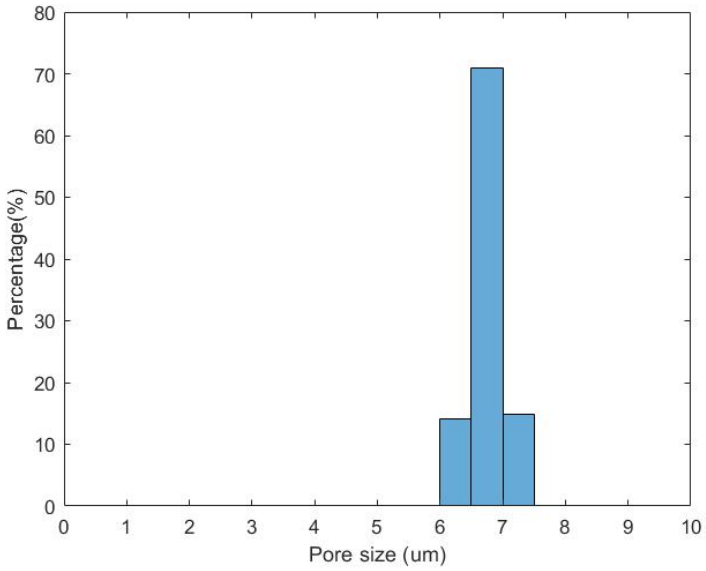

Figure 4.2: Pore size distribution of the membrane obtained via ImageJ analysis. Most pore sizes fall in the range of 6.5-7 μm, with a small percentage from 7- 7.5 and 6-6.5 μm

4.2. Contact angle and surface roughness

Due to the hydrophilic property of PEGDA[2] and the commercial PTFE membrane, we expected the membrane to show a small water contact angle in air and large contact angle of air in water. With respect to the oil phase (n-hexadecane), large contact angle in both air and water was expected.

The static contact angle (SCA) measurements were performed 5 times and the average (mSCA) was calculated. The results in Table 4.1 show that while the PEGDA membrane was not only more hydrophilic than the commercial membrane, it was also more oleophobic underwater. Both membranes absorb n-hexadecane in room environment (air). Thus, no contact angle of oil was measured in air. A few contact angle photos are provided as Figure 4.3 and Figure 4.4.

Table 4.1: Comparison of mean static contact angles (mSCA) of 3D-printed (3Dp) membranes and commercial PTFE membrane (JCWP14225) in different conditions.

TYPE	3Dp membrane mSCA [°]	commercial membrane mSCA [°]
Oil CA in water	131.96 ± 2.14	111.68 ± 2.97
Air CA in water	134.15 ± 2.41	114.63 ± 4.22
Water CA in air	45.54 ± 2.48	67.7 ± 1.13
Oil CA in air	N.A.	N.A.

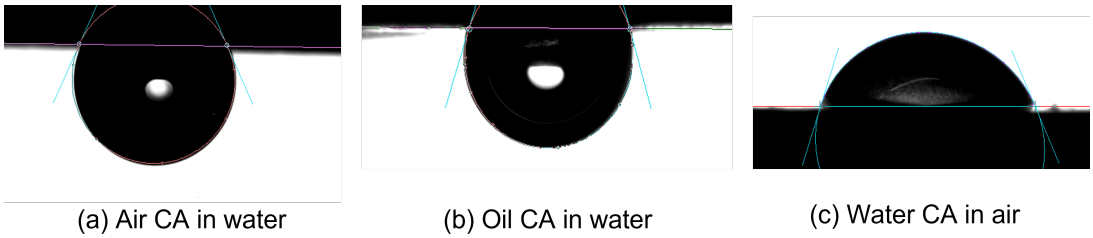

(a) Air CA in water (b) Oil CA in water (c) Water CA in air

Figure 4.3: Contact angles of different liquids in different environments on the 3D printed PEGDA membrane, as labeled in the figures. We did not include the oil contact angle in a room environment here as it is not measurable.

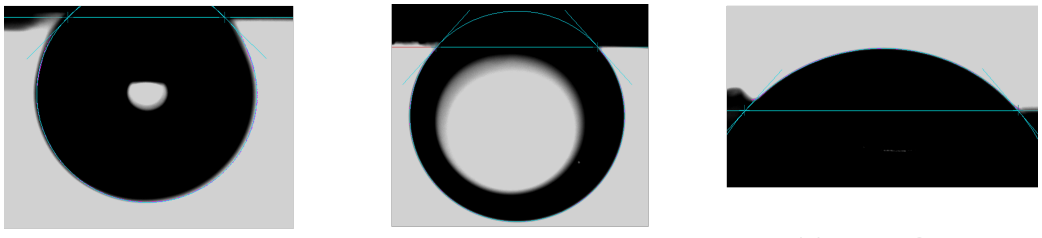

(a) Air CA in water (b) Oil CA in water (c) Water CA in air

Figure 4.4: Contact angles of different liquids in different environments on the commercial PTFE (JCWP14225) membrane, as labeled in the figures. We did not include the oil contact angle in a room environment here as it is not measurable.

The low contact angle of n-hexadecane can likely be attributed to the low surface tension of n-hexadecane. As Young's equation[3] depicts:

$$cos(\theta) = \frac{\gamma_{SA} - \gamma_{SL}}{\gamma_{LA}} \tag{4.1}$$

In which θ is the contact angle, γ_{SA} is the interfacial tension between solid and air, γ_{SL} is the interfacial tension between soild and liquid, and γ_{LA} is the interfacial tension between liquid and air. Figure 4.5 shows the definition of young's equation[4]. The low surface tension of n-hexadecane results in a low contact angle[5,6] which caused the contact angle of n-hexadecane in a room environment not to be measurable. The results do still show that both membranes are hydrophilic and underwater-oleophobic in nature, thus suitable for oil filtration from an oil-in-water emulsion.

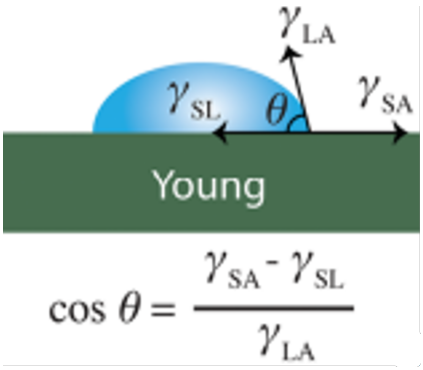

Figure 4.5: Schematic representation of young's equation, in which θ is the contact angle, γ_{SA} is the interfacial tension between solid and air, γ_{SL} is the interfacial tension between soild and liquid, and γ_{LA} is the interfacial tension between liquid and air

Only the dynamic contact angle of water in an air environment is provided. The first 3 cycles are shown in Figure 4.6. One could see that as both materials are hydrophilic, the membrane slowly absorbs water, causing the maximum and minimum contact angles to drop within each cycle[7]. The graph also shows that the 3D-printed membrane has a larger contact angle hysteresis (difference between maximum and minimum contact angle values) (44 °) than the commercial membrane (33 °), indicating a larger surface roughness[8].

To further investigate the difference between contact angle hysteresis, AFM was employed to observe the membrane surface roughness (Figure 4.7). The results show that the surface roughness values, indicated by root mean square (rms), are 451 nm and 252.2 nm for 3D-printed and commercial PTFE membranes respectively. The surface of the 3D-printed PEGDA membrane is rougher than the commercial membrane producing a more hydrophilic and underwater-oleophobic product. This is in line with previous research[8,9], which shows that a rougher surface on a nanometer scale leads to a more hydrophilic behavior and thus larger contact angle hysteresis. This also indicates that the 3D-printed membrane is a more ideal candidate for oil separation purposes than the commercial membrane.

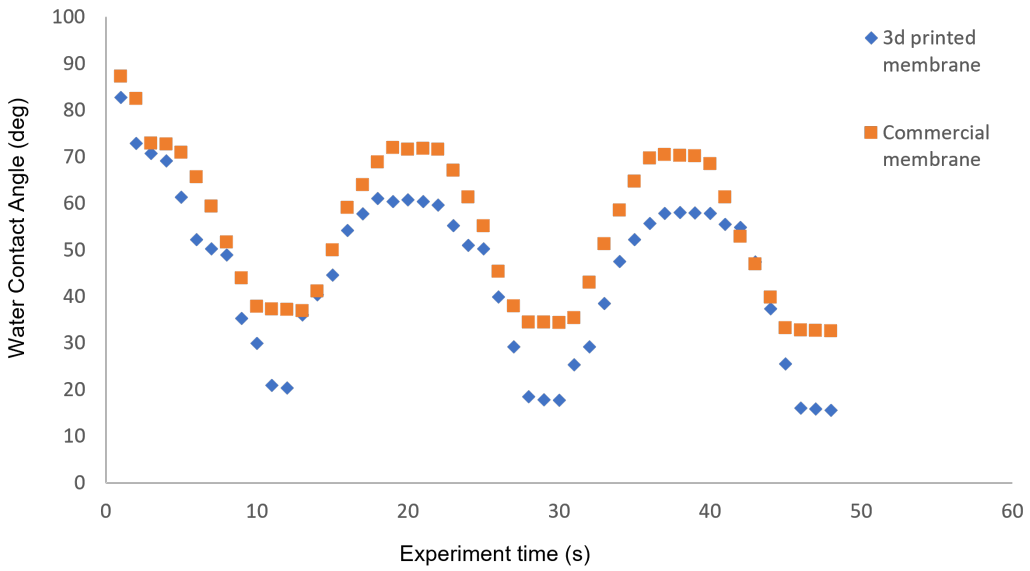

Figure 4.6: Dynamic contact angle comparison of 3D printed membrane and commercial membrane

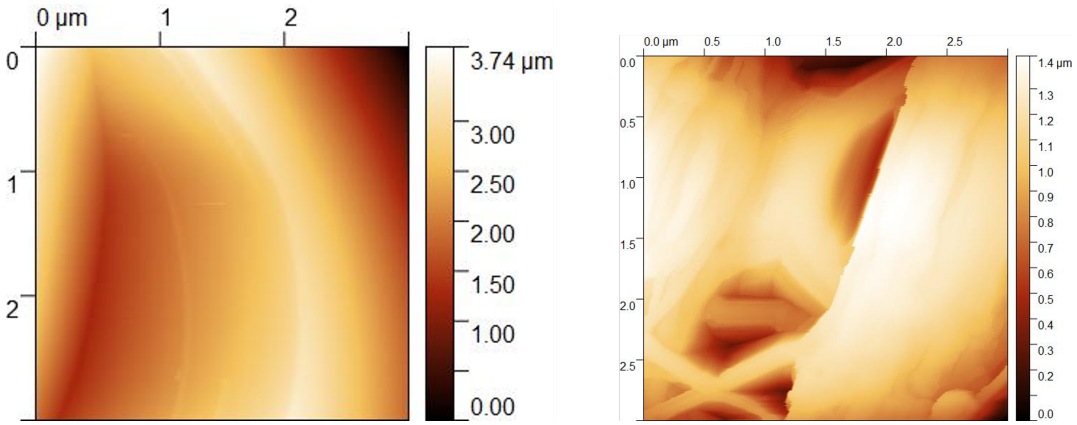

Figure 4.7: Atomic force microscopy (AFM) images comparing 3D-printed membrane (left) and commercial PTFE membrane (right). Both are imaged in tapping mode and the size of the measured area is 3μm x 3μm

4.3. Permeability Measurement

The permeability of the 3D-printed membranes was measured via a dead-end filtration device. The pressure was increased in a step-wise manner from 100 millibars to 500 millibars. The flux was recorded, and the permeability can be calculated via Darcy's law (Equation 3.3)[10]. The flux was multiplied by the viscosity of water, and the pressure gradient was calculated. We plotted the relationship, as shown in Figure 4.8, to find the slope, the slope is thus the permeability in m^2.

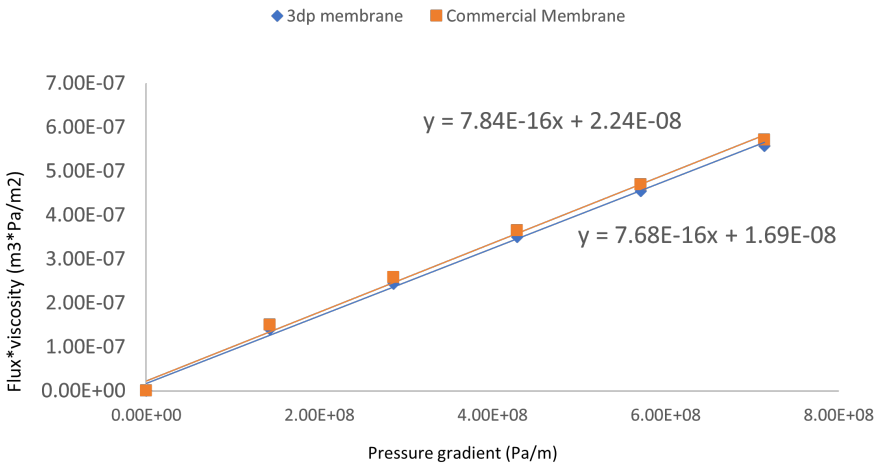

Figure 4.8: The Flux*Viscosity - Pressure gradient plot of both the 3Dp membrane and commercial membrane

The 3D-printed membrane recorded an average permeability of $7.69*10^{-16}$ m^2, while the commercial membrane recorded an average permeability of $7.84*10^{-16}$ m^2. Interestingly, despite having different porosity, the permeability and flux of the two membranes are extremely similar. The values do not match up with established permeability prediction models such as the 3D tube model[11], which is given as:

$$\kappa = \frac{\phi r^2}{8\tau} \tag{4.2}$$

In which ϕ is the porosity of the membrane, r is the pore radius, τ is the tortuosity and κ is the permeability.

Via observing the permeability at different pressures, we observed a permeability drop as a function of pressure. In other words, if we calculate the permeability for every pressure point, we see the permeability drops as pressure increases. This is further confirmed by doing the experiments at a low-pressure range of 13 millibars to 34 millibars for the 3D-printed membranes, as shown in Table 4.2 and Figure 4.9.

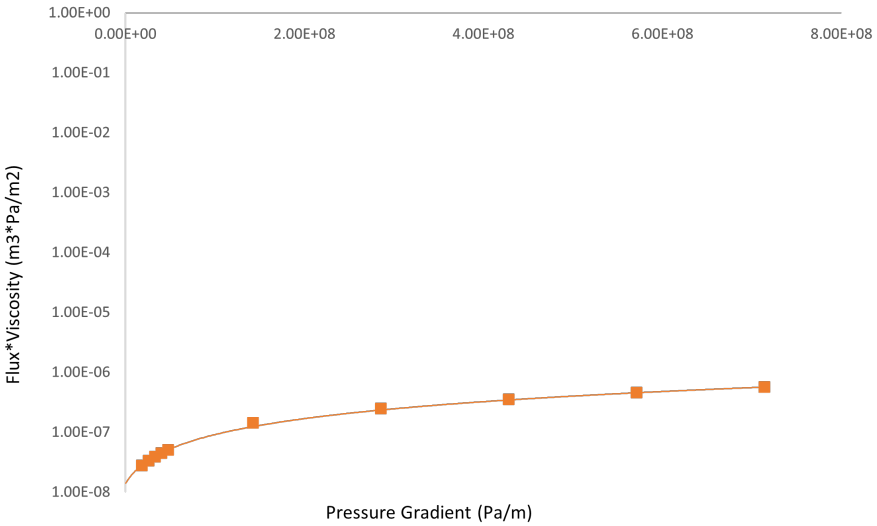

Figure 4.9: As shown in the figure, the slope (permeability) drops as the pressure gradient increases.

Table 4.2: Permeability calculations (κ) at the pressures (P) ranges of both 13 to 34 mbar and 100 to 500 mbar for the 3Dp membrane.

P (mbar)	κ (m^2)	P (mbar)	κ(m^2)
13.24	$1.46 * 10^{-15}$	100	$8.30 * 10^{-16}$
18.50	$1.25 * 10^{-15}$	200	$8.05 * 10^{-16}$
23.42	$1.15 * 10^{-15}$	300	$7.92 * 10^{-16}$
28.49	$1.08 * 10^{-15}$	400	$7.82 * 10^{-16}$
33.68	$1.03 * 10^{-15}$	500	$7.70 * 10^{-16}$

These two phenomenons: 1. Discrepancy between darcy's law and measured permeability and 2. permeability drop with pressure increasing, can be explained based on membrane compaction at high-pressure environments, which has been shown to decrease the flux when the pressure increased during permeability experiments[12]. Researchers[13,14] hypothesized that the deformation during pressurizing caused the thickness of the membrane to reduce and also caused the pores to deform[15]. The tortuosity of the membrane thus increased, which decreased the permeability of the membrane, as shown in the 3D tube model (Equation 4.2). A simplified schematic demonstrating this phenomenon is shown in Figure 4.10. Yet to this day a well-documented observation has yet to be performed.

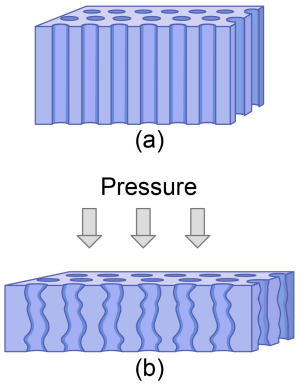

Figure 4.10: The 3D-printed membrane (a) before (b) after pressurizing. The exerted pressure deforms the cylindrical straight pores causing an increase in tortuosity.

Thus we try to perform a simple observation to verify this phenomenon. We observed the membrane in-situ using optical microscopy during permeability experiments at pressure of 100 mbar and 2000 mbar. As shown in Figure 4.11, pore deformation was observed at pressure of 2000 mbar, which proved the permeability drop due to membrane compaction.

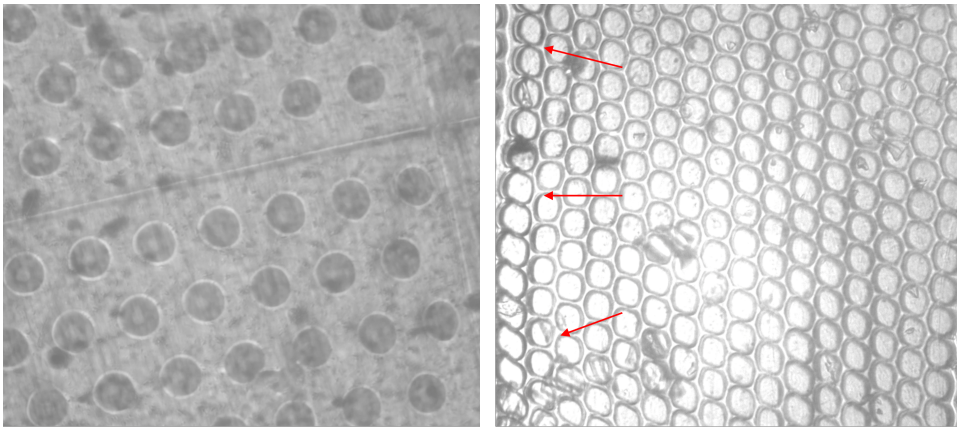

Figure 4.11: Optical microscopy images of PEGDA membrane during permeability experiments at (a) 100 mbar and (b) 2000 mbar. The membrane pores deformed under high-pressure (2000 mbar), causing tortuosity to increase and permeability to decrease. The most deformed region is shown with red arrows,

4.4. Separation Performance Study

In the separation study, the system is set at 500 mbar for 5 minutes. Both the 3D-printed membrane and the commercial benchmark membrane were tested.

The POC emulsion was first tested. The water-rich phase acted as the feed and was filtered by both membranes separately. The rejection ratio (Equation 3.4) of the benchmark PTFE membrane is recorded at 82% while the 3D-printed membrane is recorded at 22%. Using the standard emulsion in the dead-end filtration experiment, the rejection rate of the benchmark PTFE membrane is recorded at 15%, while the rejection ratio of the 3D-printed membrane is

1%.

There are two explanations for the poor rejection ratio of the 3Dp membrane. It can possibly be first explained by the fact that the pore sizes of the membrane are larger than the average droplet size of the standard emulsion, which is 3.44 μm, as shown in Figure 4.2. Due to the pore size uniformity in 3D-printed membrane, there is less chance of oil removal with this droplet size range. The commercial PTFE membrane has a non-uniform pore size distribution (Figure 4.12), which results in the possibility of rejection of the oil droplets, even if the average pore size is larger than the droplet sizes. This is reflected by the 15 % rejection ratio that we observed.

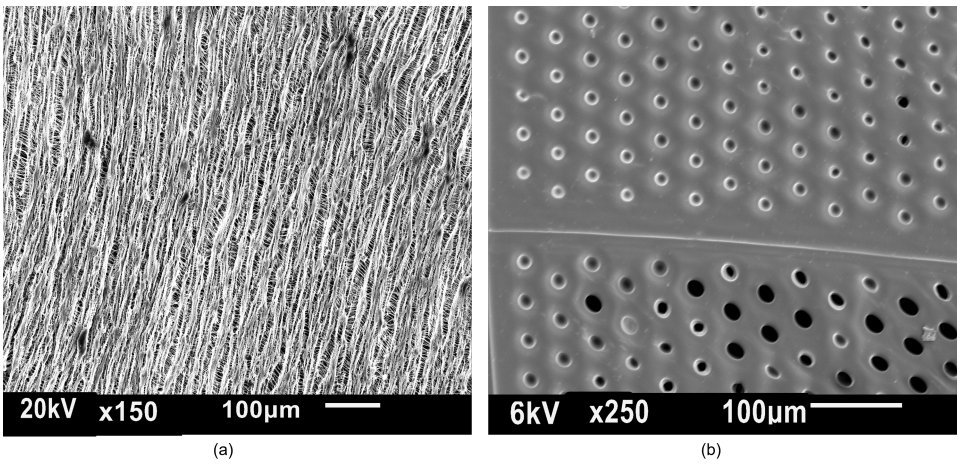

Figure 4.12: The SEM images of (a) commercial PTFE (JCWP14225) membrane showing a wide pore size distribution, and (b) 3D-printed membrane with a rather uniform pore size distribution causing a low rejection rate of the standard emulsion compared to that of the commercial PTFE membrane.

Another reason for the low rejection ratio can also come from the fact that PEGDA can be degraded by water due to hydrolysis. When placed in an environment with high water content, the ester bonds in PEGDA are susceptible to hydrolysis[16], causing the monomer chains to break up and degrade the membrane, causing some defects and perhaps more holes than we designed. This can further explain why even with the POC emulsion, even with a large droplet size as shown in Figure 4.2, the 3Dp membrane still has a relatively low rejection ratio. Alternative materials such as PEG diacrylamide (PEGDAA) can show a more robust performance under water environments. In PEGDAA the ester bond is replaced with an amide bond preventing hydrolysis[17].

References

1. Zhang, Q. *et al.* Design for the reduction of volume shrinkage-induced distortion in digital light processing 3D printing. *Extreme Mechanics Letters* **48,** 101403 (2021).
2. Son, K. H. & Lee, J. W. Synthesis and characterization of poly (ethylene glycol) based thermo-responsive hydrogels for cell sheet engineering. *Materials* **9,** 854 (2016).
3. Young, T. III. An essay on the cohesion of fluids. *Philosophical transactions of the royal society of London,* 65–87 (1805).
4. Bazyar, H., Moultos, O. A. & Lammertink, R. G. A review on nature-inspired gating membranes: From concept to design and applications. *The Journal of chemical physics* **157,** 144704 (2022).
5. Männel, M. J., Weigel, N., Hauck, N., Heida, T. & Thiele, J. Combining hydrophilic and hydrophobic materials in 3D printing for fabricating microfluidic devices with spatial wettability. *Advanced Materials Technologies* **6,** 2100094 (2021).
6. Hensel, R. *et al.* Tunable nano-replication to explore the omniphobic characteristics of springtail skin. *NPG Asia Materials* **5,** e37–e37 (2013).
7. Wang, Z. & Wallach, R. Effects of time-dependent contact angle on wettability of sub-critically water-repellent soils. *Water Resources Research* **56,** e2020WR027314 (2020).
8. Müller, B. *et al.* Impact of nanometer-scale roughness on contact-angle hysteresis and globulin adsorption. *Journal of Vacuum Science & Technology B: Microelectronics and Nanometer Structures Processing, Measurement, and Phenomena* **19,** 1715–1720 (2001).
9. San-Miguel, A. & Behrens, S. H. Influence of nanoscale particle roughness on the stability of pickering emulsions. *Langmuir* **28,** 12038–12043 (2012).
10. Darcy, H. *Les fontaines publiques de la ville de Dijon* (V. Dalmont, 1856).
11. Gruener, S., Wallacher, D., Greulich, S., Busch, M. & Huber, P. Hydraulic transport across hydrophilic and hydrophobic nanopores: Flow experiments with water and n-hexane. *Physical review E* **93,** 013102 (2016).
12. Wu, Y.-H., Park, H. B., Kai, T., Freeman, B. D. & Kalika, D. S. Water uptake, transport and structure characterization in poly (ethylene glycol) diacrylate hydrogels. *Journal of Membrane Science* **347,** 197–208 (2010).
13. Parker, K., Mehta, R. & Caro, C. Steady flow in porous, elastically deformable materials (1987).
14. Persson, K. M., Gekas, V. & Trägårdh, G. Study of membrane compaction and its influence on ultrafiltration water permeability. *Journal of membrane science* **100,** 155–162 (1995).
15. Dehghan, R. & Barzin, J. High cut-off membrane: evaluation of pore collapse and the synergistic effect of low and high molecular weight polyvinylpyrrolidone. *Journal of Polymer Research* **28,** 1–19 (2021).

16. Stillman, Z., Jarai, B. M., Raman, N., Patel, P. & Fromen, C. A. Degradation profiles of poly (ethylene glycol) diacrylate (PEGDA)-based hydrogel nanoparticles. *Polymer Chemistry* **11,** 568–580 (2020).

17. Browning, M., Cereceres, S., Luong, P. & Cosgriff-Hernandez, E. Determination of the in vivo degradation mechanism of PEGDA hydrogels. *Journal of Biomedical Materials Research Part A* **102,** 4244–4251 (2014).

5

Conclusion

In this work, we showcased for the first time the fabrication of a 3D-printed membrane via novel dual-wavelength 3D printing technology. During the process of the research, as outlined in chapter 3, the printing procedure was extensively restudied. Firstly, the cell was redesigned to make the thickness of the cell stable. Secondly, the printing scheme was adjusted to print the support first then the whole membrane, which results in a 3D-printed product with an even thickness along the width. Last but not least, a heating procedure to increase the mechanical integrity of the membrane was introduced. With this modified printing procedure, reproducible membranes with sub-10 micron pores were successfully produced.

The SEM images of the membranes further revealed that the pore sizes were smaller than our designed 10 μm diameter, falling into the range of 6-7μm, which is a 30 to 40% pore size reduction. As discussed in chapter 4, this is caused by over-polymerization at the edge of the pore, which resulted in a smaller pore radius than designed. This indicates that the system can produce membranes with smaller pores than 10μm, but can risk overpolymerization, which results in no pores in the membrane.

The membrane exhibited a high underwater oil contact angle, which indicates a good oil-repellent property, making it suitable for separating large oil droplets in an oil-water emulsion. The surface roughness of the measured membrane further confirms the good oil-repellent property, as the microscale surface roughness of the 3D-printed membrane is substantially higher than the benchmark membrane.

Another interesting point of this research is the fact that the material of PEGDA presents its own challenges when used in 3D printing of membranes. During this research, the local swelling created cracks in the membrane, which caused major issues in characterization. This was solved by a quick fix of preserving the membrane in water, which while inevitably caused the whole decomposition of the membrane, experiments were able to be performed. The PEGDA membranes also demonstrated compaction under high pressure, which resulted in an unpredictable permeability. The filtration performance of the membrane is currently less than satisfying, likely due to two reasons: the size of the pores is too large for the droplet size, and also degradation of the membrane during preservation.

All in all, a microfiltration membrane was successfully manufactured via a novel 3D printing method based on dual-wavelength stereolithography. It satisfies the basic requirement of being capable of filtration and indicates good potential for enhancement. Further research and improvements in the materials department can further enhance the manufacturing method to make it a more viable candidate for producing membranes.

6

Future Work and Recommendations

In this chapter, we will discuss further directions for this domain of research. Hopefully, as future research enhances, this method can be used for mass membrane manufacturing.

As one of the characterization methods, the permeability of membranes is measured to obtain the transportation rate of the passing fluids. This is useful for understanding the requirements for a membrane to be operational[1], such as the operating pressure range and the expected permeate flow rate, which is useful for processing equipment design[2].

However, we observed membrane compaction during permebaility experiments under high pressure. This led to the membrane permeability drop with increase in pressure, causing Darcy's law to fail to predict the permeability. This further eliminates the possibility of predicting the operational requirements of the membrane such as permeability in a 3D-printed membrane with uniform and cylindrical pore size. Although we have provided a rough observation of the phenomenon and the results indicate that indeed pore compaction takes place, it will be beneficial to dedicate resources to research the compaction of PEGDA and other polymers under high-pressure environments.

Another point of interest is the chosen material for 3D printing. As discussed in chapter 4, PEGDA might not be the most suitable material for a membrane, as membranes stay in a water-based environment for a long time, and hydrolysis can take place causing deterioration of the membrane structures[3]. PEG-diacrylamide (PEGDAA) is a suitable starting candidate for replacement[4] as it has the most similar property as PEGDA while having the benefit of being less susceptible to hydrolysis.

All in all, we have showcased the dual-wavelength 3D printing method is suitable for manufacturing membranes We envision that it can be used for a variety of biomedical purposes. One example is cell aggregation filtration. Cell aggregation filtration requires membranes with exact and uniform pore size distribution to effectively filter single tissue cells for further analysis and characterization[5], a microchip for this purpose is shown as Figure 6.1. Due to the mono-dispersed range of tissue cells, which is concentrated in the range of 7-8 μm, normal membranes can cause the filtration efficiency to drop as it removes some of the desired single tissue cells due to its wide pore size range. This is where our membrane can play a more significant role in increasing filtration efficiency. Another purpose for these membranes is the

removal of large bacteria from groundwater[6,7], As groundwater serves as drinking water and is increasingly contaminated by urban wastewater with bacteria, the need for removing bacteria from groundwater has become more important. Our membrane production method provides a simple yet effective way of manufacturing means for reducing waterborne disease transmission.

This method of manufacturing membranes also provides a pathway for the simple manufacturing of conical pore membranes, however, it has difficulties making membranes with sub-5 micron pores. We envision the membranes with conical pores can replace the need for a porous support[8], since they will still have a strong foundation compared to our current membranes. It will also have the benefit of having in effect a small pore size, as these small particles will get stuck in the pores. This can expand the usage of these 3D-printed membranes as they will be more suitable for more filtration applications such as oil-water emulsion separation, which we had showcased has a droplet size of circa 2-3 μm. We have already shown that this membrane is possible to print, yet further optimization still needs to be performed.

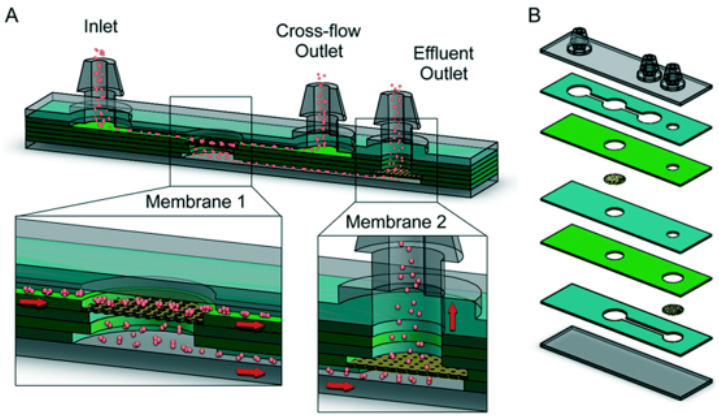

Figure 6.1: The tissue cell filtration microchip designed by Qiu et al[5], the membranes in the chip are used to filter small monodispersed tissue cells.

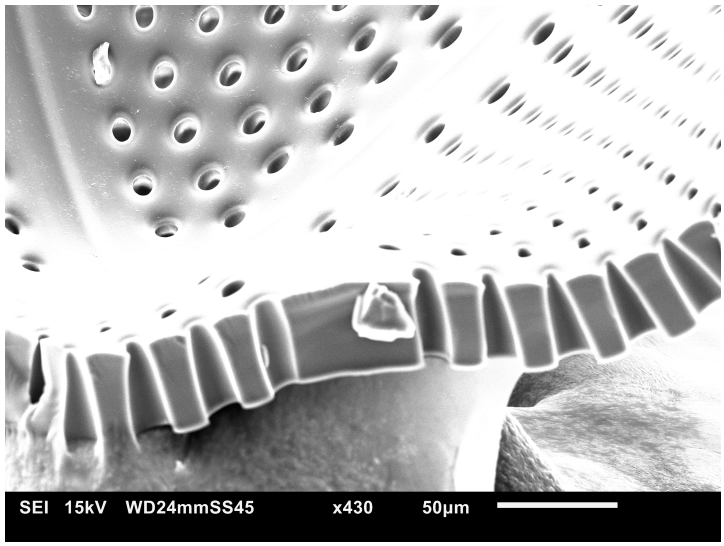

Figure 6.2: The conical pore membranes, the side with smaller pores has higher mechanical integrity and the possibility of blocking smaller particles, such making filtration of smaller particles possible.

References

1. Popham, N. Resin infusion for the manufacture of large composite structures. *Marine Composites: Design and Performance; Pemberton, R., Summerscales, J., Graham-Jones, J., Eds,* 227–268 (2019).
2. Singh, R. Water and membrane treatment. *Membrane Technology and Engineering for Water Purification* **2,** 81–178 (2015).
3. Browning, M., Cereceres, S., Luong, P. & Cosgriff-Hernandez, E. Determination of the in vivo degradation mechanism of PEGDA hydrogels. *Journal of Biomedical Materials Research Part A* **102,** 4244–4251 (2014).
4. Browning, M. B. & Cosgriff-Hernandez, E. Development of a biostable replacement for PEGDA hydrogels. *Biomacromolecules* **13,** 779–786 (2012).
5. Qiu, X. *et al.* Microfluidic filter device with nylon mesh membranes efficiently dissociates cell aggregates and digested tissue into single cells. *Lab on a Chip* **18,** 2776–2786 (2018).
6. Goswami, K. P. & Pugazhenthi, G. Credibility of polymeric and ceramic membrane filtration in the removal of bacteria and virus from water: A review. *Journal of environmental management* **268,** 110583 (2020).
7. Hosseini, S. S., Khodadadi, H. & Bakhshi, B. Fabrication, tuning and performance analysis of polyacrylonitrile (PAN)-derived microfiltration membranes for bacteria removal from drinking water. *Korean Journal of Chemical Engineering* **38,** 32–45 (2021).
8. Bouzerara, F., Harabi, A., Achour, S. & Larbot, A. Porous ceramic supports for membranes prepared from kaolin and doloma mixtures. *Journal of the European Ceramic Society* **26,** 1663–1671 (2006).

A

Appendix

A.1. Procedure on 3D printing membrane

Pre-printing

1. Clean the top glass (24x24 mm^2, Brand, Germany) and bottom glass (76x26 mm^2, Brand, Germany) with acetone using precision wipes, then air-dried via a lab-sized high-pressure blow.
2. Prepare a solution mix of photopolymer resin and spacer beads of 70 μm (Micropearl SP series, Sekisui Chemical Co., Ltd, Japan) with a concentration of 0.0033 g/1 ml. When observed under a 10x lens, there should be circa 3 to 4 particles per frame.

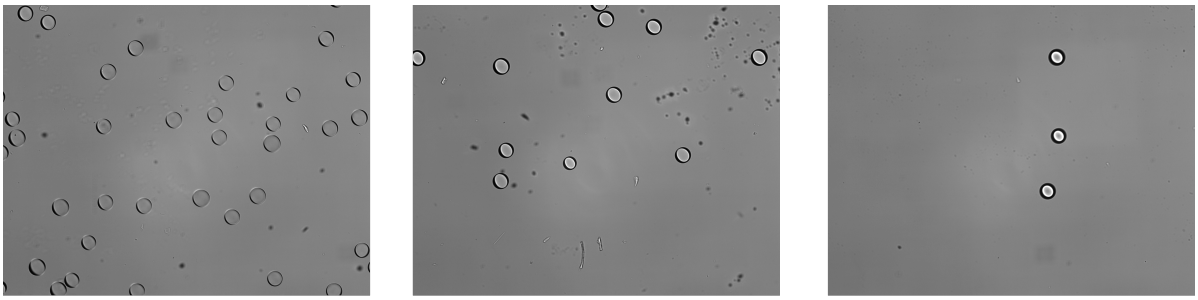

Figure A.1: (a) concentration of 0.02g/1ml (b) concentration of 0.01g/1ml (c) 0.0033g/1ml

3. Dot 4 dots of the mix to the four corners of the top glass, and cover the top glass on the bottom glass. The figure was provided as Figure 3.5, it is provided here again for ease of reference.

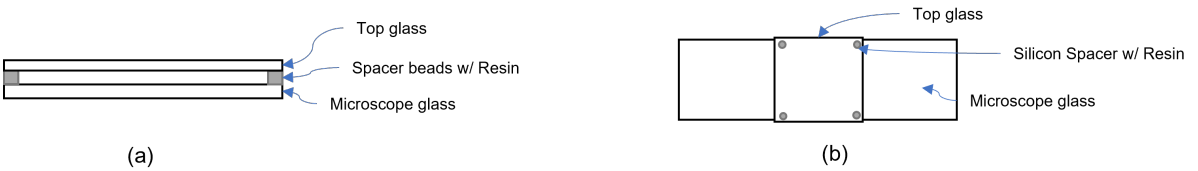

Figure A.2: (a) The side view of the cell (b) The top view of the cell

4. Supply 50 μl of printing resin from the side, the surface tension of the two glass surfaces will fill the vacancy in between automatically. It is advised to do this as the author has found if the 50 μl resin is covered directly from the top, resin cannot be guaranteed to fill in fully, causing thinner membranes to be printed and can cause the product to break easily.
5. After filling the printing cell, it can be moved for printing.

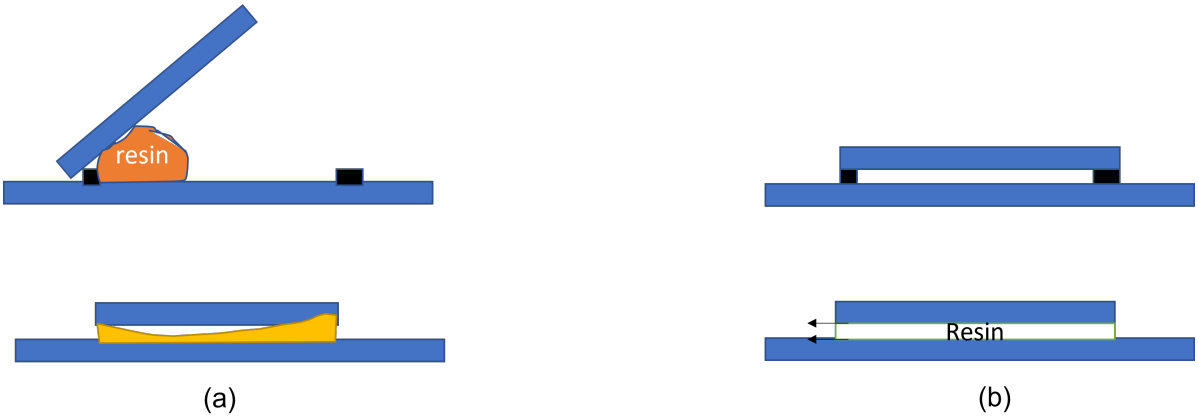

Figure A.3: (a) Glass is covered from the top with 50μl resin. A vacancy can be created causing thinner membranes to be printed. (b) The resin is filled with a pipette from the side, the resin vacancy will disappear with this filling technique.

Printing

6. As the printing starts from the bottom to the top (as in, the stage moves downwards when printing every tile), focus on the top of the bottom glass. The printing procedure can then be started as soon as the printer reads in the calculation file. The user may test for a few single tile prints, it might be the case the user will have to adjust the position of the stage a few micrometers to get a fine print. A fine print should have clearly defined features.
7. If the user is satisfied, the printing procedure can start. After printing, the cell can be removed for post-processing.

Post-printing

8. Carefully wash the whole cell with solvent first, then take apart the cell via a spatula and remove the 3D-printed membrane(s) from the cell.
9. Put the membrane in a solvent bath and sonicate the bath for 20 minutes. Set up the bath similar to as Figure A.4.
10. Remove the membrane from the sonicator and solvent bath. With two filters, one on top and another on the bottom, press the membrane with a weight and heat the membrane up to 160 °C for 20 minutes.
11. Remove the membrane from the heater and this is the product. Conserve the membrane in water for further observation.

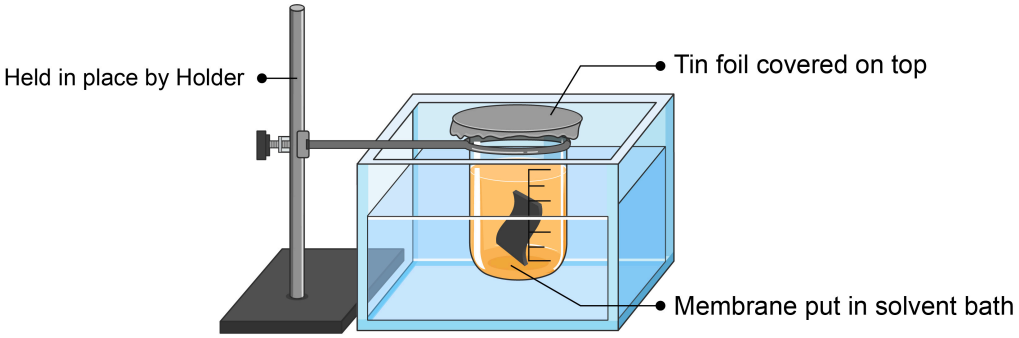

Figure A.4: The membrane(s) is put in a solvent bath filled in a beaker. Sonicate the beaker in a sonicator for 20 mins.

A.2. Analyzing the pore diameter of the printed membranes

In this section, we showcase the procedure of measuring the pore diameter via Image J and MATLAB, the MATLAB program code will be supplemented in section A.3.

1. The desired SEM image is first opened in ImageJ and calibrated, the scale of the picture is set.

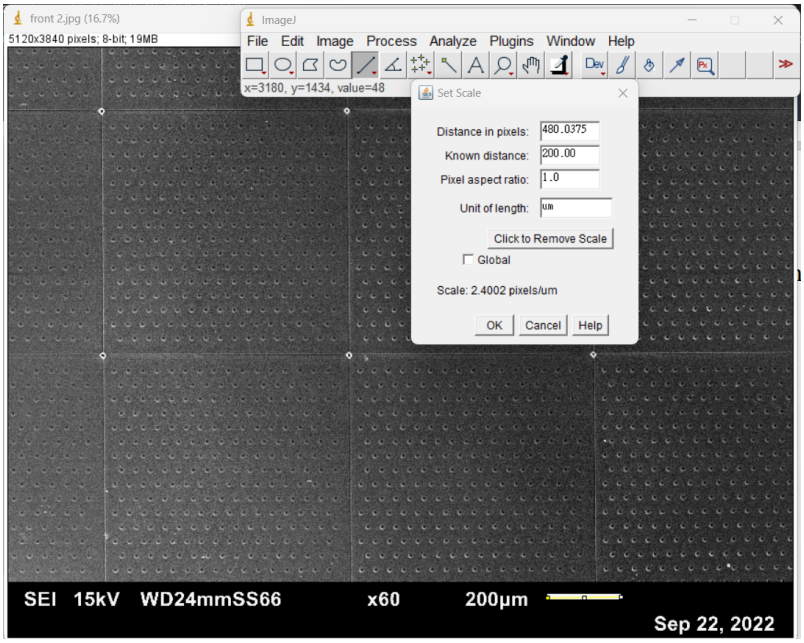

Figure A.5: Scale of picture is first set

2. Next, the image is enlarged via duplication of a single tile of the picture. A bandpass filter is applied to evenly illuminate the figure.

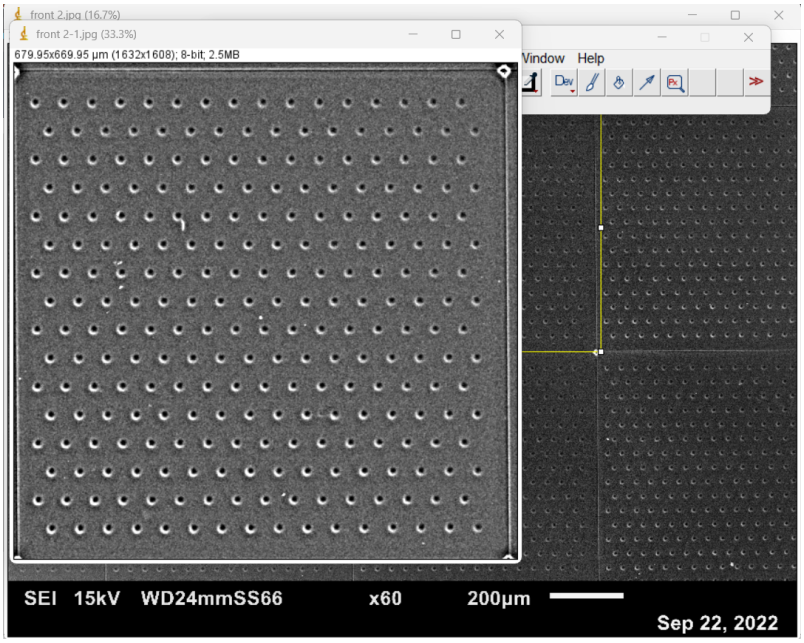

Figure A.6: Bandpass filter is applied to the figure

3. Next, we threshold the image into black pores and white background, we also remove noise at this point.

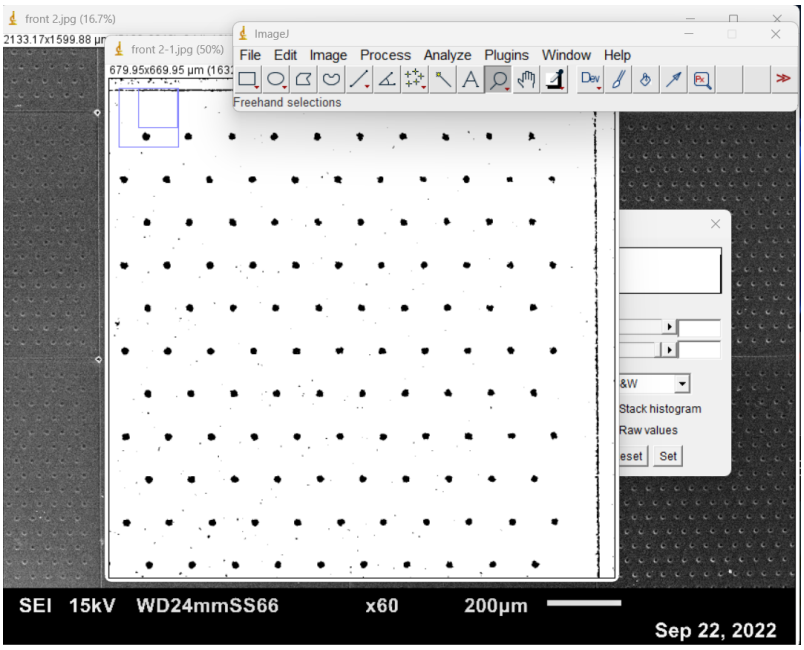

Figure A.7: Threshold applied to figure

4. Using the analyze particles function, we can arrive at an area that is calculated with the units of micrometer square.

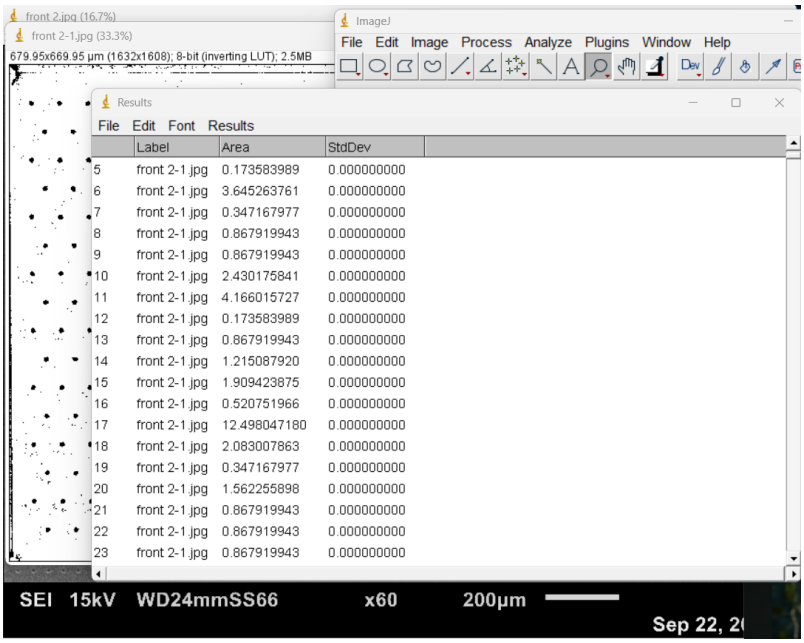

Figure A.8: Area is automatically calculated

5. Using the following function, we are able to calculate the diameter of the pores:

$$D = 2\sqrt{\frac{A}{\pi}} \tag{A.1}$$

6. The diameters are then input into a CSV file, then organized into bar charts via a self-made Matlab program provided in section A.3.

7. Finally, the pore size binning chart can be produced, we thus know the range of pore sizes of the 3D printed membrane.

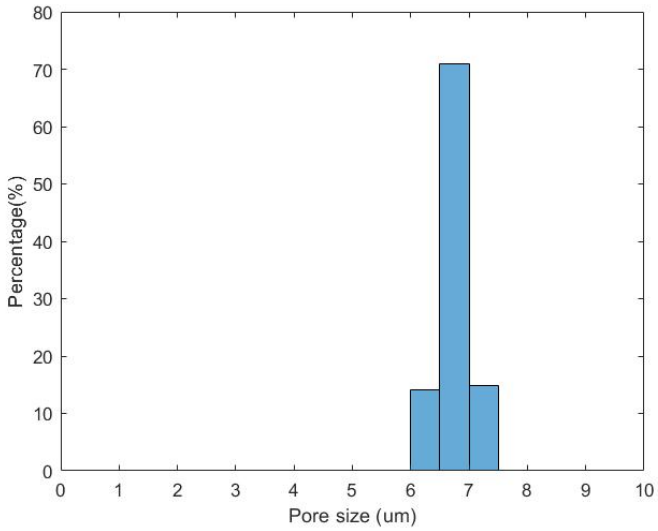

Figure A.9: The pore size distribution of the 3D-printed membrane analyzed via this method

A.3. Matlab program for organizing pore sizes

```
clear;
clc;
%% Program is manual
%reading data, diameter
d=xlsread('Pore size distribution.csv','d:d');
% deleting noise, manual
d(d < 5) = [];
%% First Part, check what is the range of our data?

%define edges
edges=linspace(5,10,(10-5)*2+1);
%binwidth=0.5;
% plot histogram
histogram(d,"binedge",edges,'normalization','probability');
%histogram(d,256);

% setting histogram limits
xlim([0,10]);
xlabel('Pore size (um)');
yticklabels(yticks*100);
ylabel('Frequency(%)');
%}
```

A.4. Filtration Performance Measurement

We outline in this section the method of filtration performance measurement. We show here using photos of the standard emulsion, the procedure is completely the same for the POC emulsion.

After the preparation of the emulsion, different concentrations of the emulsion were made and filled in flow cells. We first take the ”blank cell” and ”full cell” (only solvent and only emulsion, respectively) and do a sweeping mode, which will tell us the best wavelength for UV-VIS measurement.

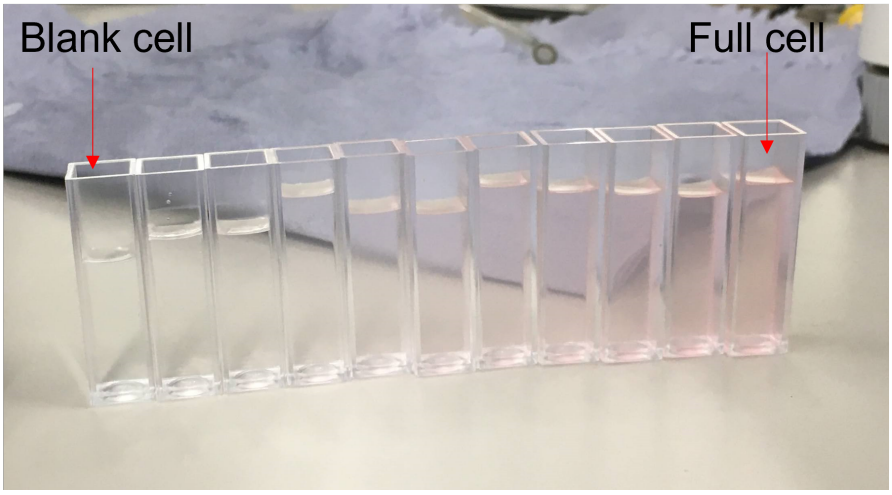

Figure A.10: Emulsions of different concentrations filled in flow cells. The blank and full cell are specifically pointed out as they are used for first calibration.

We then use the single wavelength mode, in the standard emulsion case, at 520 nm, to measure the absorbance. After measuring absorbance, a concentration-absorbance relation plot can be plotted, as shown in Figure A.11. With this, we can then measure the absorbance from the permeate and calculate the concentration, this will then give us the rejection ratio.

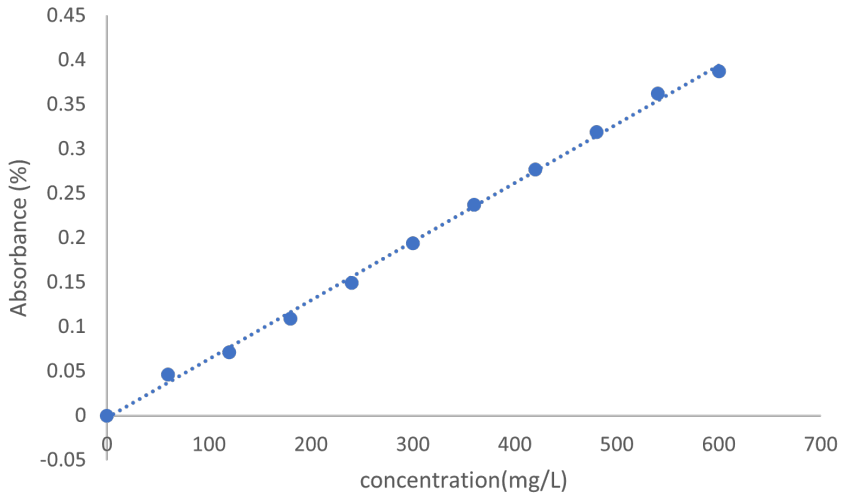

Figure A.11: The concentration/absorbance relationship plot